

**A SINGULARITY-FREE MECHANISM
FOR HOLONOMIC ORIENTATION
CONTROL OF A SPHERICAL
PERMANENT MAGNET**

by

Samuel E. Wright

A thesis submitted to the faculty of
The University of Utah
in partial fulfillment of the requirements for the degree of

Master of Science

Department of Mechanical Engineering

The University of Utah

December 2014

Copyright © Samuel E. Wright 2014

All Rights Reserved

The University of Utah Graduate School

STATEMENT OF THESIS APPROVAL

The thesis of _____ **Samuel E. Wright** _____

has been approved by the following supervisory committee members:

_____ **Jake Abbott** _____, Chair _____ **8/15/14** _____
Date Approved

_____ **Stephen Mascaro** _____, Member _____ **10/10/14** _____
Date Approved

_____ **Kam Leang** _____, Member _____ **8/15/14** _____
Date Approved

and by _____ **Tim Ameel** _____, Chair/Dean of

the Department/College/School of _____ **Mechanical Engineering** _____

and by David B. Kieda, Dean of The Graduate School.

ABSTRACT

Untethered magnetic devices such as magnetic capsule endoscopes, magnetic swimming microrobots, and magnetic screws, as well as tethered magnetic devices such as magnet-tipped catheters and magnet-tipped cochlear-implant electrode arrays, can be actuated by a single permanent magnet positioned in space by a robotic manipulator. Free positioning of the actuator magnet, however, may require the robotic manipulator to enter unfavorable configurations (e.g., kinematic singularities). This thesis presents a three degree-of-freedom mechatronic device that rotates a spherical, or spherically encapsulated, permanent magnet for the control of remote magnetic devices. We refer to the device as the spherical-actuator-magnet manipulator (SAMM). The SAMM, which is designed to replace or augment the singularity-prone spherical wrist used by prior permanent-magnet manipulation systems, utilizes three omniwheels that enable holonomic control of the spherical magnet's heading and allows the magnet's instantaneous axis-of-rotation to be set arbitrarily. The SAMM can perform closed-loop control of the spherical actuator magnet's dipole (i.e., the vector pointing from the south to the north magnetic poles, whose magnitude defines the magnet's strength). The orientation of the magnetic dipole is estimated on-line using a hybrid extended Kalman filter, which fuses a dynamic model of the device and incremental optical encoders mounted to the driving motors. This thesis documents the design, assembly, state estimation, and control of the prototype SAMM.

CONTENTS

ABSTRACT	iii
ACKNOWLEDGMENTS	vi
CHAPTERS	
1. INTRODUCTION	1
2. THEORY OF OPERATION	4
2.1 Velocity Kinematics and Inverse Kinematics	4
2.2 Detecting the Magnet's Dipole Moment	6
3. PROTOTYPE IMPLEMENTATION	10
3.1 Omniwheels	12
3.2 Compliance for Magnet and Omniwheel Irregularities	15
3.3 Hall-Effect Sensor Cluster	17
3.4 System Integration	18
4. STATE ESTIMATION	21
4.1 Review of the Hybrid Extended Kalman Filter	21
4.1.1 Predict	22
4.1.2 Update	22
4.2 Implementing the Hybrid Extended Kalman Filter	23
4.2.1 Dynamics	23
4.2.2 Sources of Imprecision	24
4.2.2.1 Measurement Noise	24
4.2.2.2 Process Noise	25
4.2.3 Hybrid EKF Implementation for the SAMM	25
4.2.4 Numerical Integration	27
5. CONTROL	28
5.1 Pointing-Mode Controller	29
5.2 Rotating-Mode Controller	29
6. EXPERIMENTATION	32
6.1 Parameter Estimation	33
6.1.1 Coulomb and Viscous Friction	33
6.1.2 Sensor Noise	33
6.1.3 Process Noise	35
6.2 Controller Tuning	35

6.2.1	Ziegler-Nichols Tuning of the Heading Controllers	35
6.2.2	Tuning of the Angular-Velocity Controller	37
6.3	Performance Demonstrations	38
6.3.1	Pointing Mode	38
6.3.2	Rotating Mode	43
7.	DISCUSSION	47
7.1	Spherical-magnet Substitution	47
7.2	Application-specific Tuning of the Gear Ratio η	47
7.3	Omniwheel Orientations	48
7.4	Potential Performance Improvements	48
7.4.1	SAMM Components	49
7.4.2	Further Empirical Tuning	49
8.	CONCLUSION	50
	REFERENCES	51

ACKNOWLEDGMENTS

I would like to thank Dr. Jake Abbott for inspiring and enabling me. I would also like to thank Dr. Art Mahoney for his support, guidance, and friendship throughout the development of this work, as well as the rest of the Telerobotics Lab for tirelessly tolerating my humor. Finally, I would like to thank my wife Rachel for her motivation, love, and support.

This work was supported by the National Science Foundation under Grant 0952718 and by Given Imaging.

CHAPTER 1

INTRODUCTION

The potential impact in the field of minimally invasive medicine has fueled research into untethered magnetic devices (UMDs). These devices, including magnetic microrobots [1] and magnetically actuated capsule endoscopes [2], typically take the form of a mechatronic or MEMS devices with a rigidly attached magnetic body on which magnetic forces and torques are applied by an external field. Actuating UMDs, ranging in size from the microscale to the mesoscale, by pulling using magnetic forces [3,4], rolling on a surface [5–7], swimming through a fluid or crawling through a lumen via helical propulsion [8–12], and screwing through soft tissue [13] have been previously demonstrated.

The ability to control UMDs using a single rotating permanent magnet as the “actuator magnet” has previously been shown by Mahoney and Abbott [14], who demonstrated that a rotating UMD can be propelled in a lumen by a single actuator magnet. Unlike prior work, the results of [14] enable the actuator magnet to be placed in any position relative to the UMD, provided a specific position-dependent actuator-magnet rotation axis is established. A closed-form solution for the necessary actuator-magnet rotation axis that achieves a desired field rotation axis at the UMD’s position is known [14]. In the experimental results of [14], the actuator magnet was rotated by a single DC motor that was rigidly mounted to the tool frame of an industrial six-degree-of-freedom (6-DOF) robotic manipulator. In this setup, the rotation axis of the actuator magnet is fixed with respect to the tool frame of the robotic manipulator. Such a setup is capable of placing the actuator magnet with the correct rotation axis to guide a UMD through relatively simple trajectories. However, when tasked with navigating a UMD through tortuous paths (e.g., the small intestines), the physical constraints of the robotic manipulator (i.e., joint limits and singularities) limit how the UMD can be actuated.

The effects of manipulator limitations on UMD actuation are clearly demonstrated by Mahoney and Abbott in [15,16], where a single, nonrotating permanent magnet is used to levitate a semibuoyant magnetic capsule with 5-DOF (3-DOF position and 2-DOF heading)

control in a task reminiscent of stomach capsule endoscopy. In [16], kinematic singularities and workspace limitations are identified as the primary limiting factors to device actuation. To mitigate the effect of singularities, the authors introduce a control method that sacrifices control authority over the capsule’s heading in order to maintain 3-DOF control over the capsule’s position when the manipulator nears a kinematic singularity.

Aside from actuating UMDs, applications where *tethered* magnetic devices must be actuated through tortuous pathways will also be hindered by the manipulator’s limitations. Such applications include applying force and torque to a magnet-tipped catheter in the human vasculature [17] and to a magnet-tipped cochlear-implant electrode array in the human cochlea [18].

This thesis presents a mechatronic device, which we refer to as the spherical-actuator-magnet manipulator (SAMM), that enables holonomic singularity-free control of a spherical magnetic body’s orientation, to act as the actuator magnet in a magnetic manipulation system (Fig. 1.1). The SAMM is intended to be mounted to the tool frame of a robotic manipulator so as to remove previously mentioned limitations induced by the robotic manipulator; however, the SAMM could also be used in a stand-alone fashion. The SAMM consists of a spherical permanent magnet that is driven by three omniwheels that contact the spherical magnet’s surface. An omniwheel is a common mechanism that incorporates small rollers that permit controlled rotation about the omniwheel’s rotation axis and free rotation about the two orthogonal axes. Designing the three omniwheel rotation axes to be linearly independent enables any instantaneous magnet rotation axis to be achieved. By making the magnet’s axis-of-rotation continuously variable, irrespective of the robotic manipulator used to position the SAMM, the workspace constraints of the robotic manipulator are avoided. This leaves the robotic manipulator free to position the actuator magnet optimally for manipulation. This device enables robotic manipulators with less than 6-DOF to be considered for positioning (e.g., 3-DOF or 4-DOF gantry and SCARA robots) with the same level of manipulability.

There are several reasons for actuating a magnet of spherical geometry. Firstly, being of constant radius, it is simple to maintain form-closure of a spherical body regardless of its orientation, allowing it to be easily incorporated into a physical device. Secondly, a spherical magnet makes the best use of available space in the sense that it fully utilizes the volume of its bounding sphere. Thirdly, the field of a spherical magnet is theoretically perfectly fit by the analytical point-dipole model. Finally, a homogeneous spherical body has no principle directions of inertia, giving it isotropic dynamic properties.

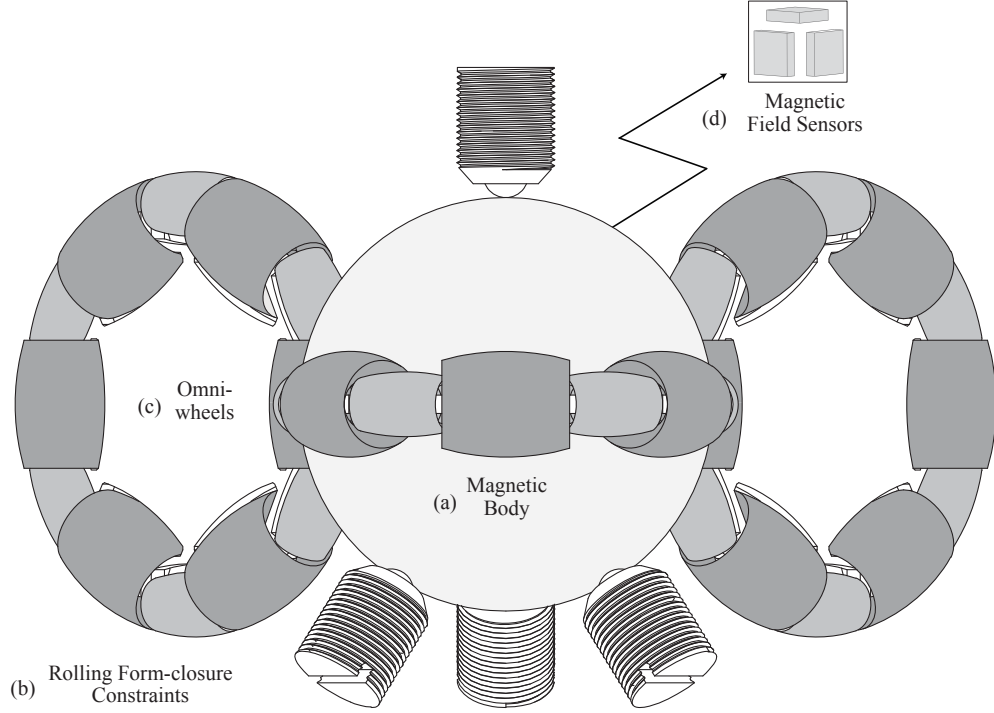


Figure 1.1. Key components of the SAMM are identified. A holonomic mechanism that rotates a spherical magnetic body (a) that is prevented from translating by four constraints (b) that create a rolling form closure. Three omniwheels (c) whose axes of rotation span \mathbb{R}^3 contact the magnetic body and cause it to rotate as desired. Magnetic field sensors (d) measure the magnetic body’s dipole moment to be used for closed-loop control of the dipole’s orientation.

Our SAMM design was inspired by previously demonstrated “ballbot” systems, in which a robot balances itself atop a sphere (e.g., a soccer ball), and controllers are used to stabilize and propel the robot [19–21]. With ballbots, only the instantaneous angular velocity of the ball is important for control, and the ball’s orientation is not measured [22] (i.e., there is no preferred “north pole” of a soccer ball). However, for the control of a spherical permanent magnet, knowledge of the magnet’s dipole heading is critical, both for controlling the dipole’s angular velocity as well as for orientation-control of the dipole itself for nonrotating tasks. Because knowledge of the dipole’s heading is critical for the SAMM to function, the SAMM includes a magnetic-field sensing unit comprising three or more Hall-effect sensors to estimate the dipole heading (we say “heading” since the dipole’s magnitude is assumed to be constant and known). The integrated system comprising the spherical magnet, the omniwheels, the actuation system for the omniwheels, the sensor system, and the necessary mechanical support structure are referred to as the SAMM throughout this document.

CHAPTER 2

THEORY OF OPERATION

The SAMM consists of a spherical magnet (Fig. 1.1(a)) that rotates freely but is prevented from translating in space by rolling form-closure constraints (Fig. 1.1(b)). The magnet is contacted by three omniwheels (Fig. 1.1(c)), which actuate the permanent magnet, making it rotate according to some desired input. The omniwheels employed on the SAMM are miniaturized, nonmagnetic, continuous-contact omniwheels, modified from the designs in [19, 23, 24], which are depicted in Fig. 1.1. The omniwheels contact the magnet with rollers that generate high friction in the driving direction while allowing the magnet to passively roll orthogonal to the drive direction with minimal friction. The speed at which each omniwheel must rotate is determined by the desired angular velocity $\boldsymbol{\omega}_{\mathbf{m}} \in \mathbb{R}^3$ of the magnet, which is set by some external control system or user input. While the magnet rotates, a sensor system that measures the magnetic field (Fig. 1.1(d)) is used to determine the spherical magnetic body's dipole moment vector $\mathbf{m} \in \mathbb{R}^3$ (i.e., the vector from the south to north magnetic poles). The measured dipole moment vector is used for closed-loop control.

2.1 Velocity Kinematics and Inverse Kinematics

For some desired angular velocity $\boldsymbol{\omega}_{\mathbf{m}}$ of the spherical magnet, the necessary omniwheel rotation speeds must be determined. Let the unit-length vectors $\hat{\mathbf{d}}_1$, $\hat{\mathbf{d}}_2$, and $\hat{\mathbf{d}}_3$ point from the spherical magnet's center to the contact point where each of the three omniwheels touches the magnet. We assume that the omniwheel axes $\hat{\mathbf{a}}_1$, $\hat{\mathbf{a}}_2$, and $\hat{\mathbf{a}}_3$ are perpendicular to $\hat{\mathbf{d}}_1$, $\hat{\mathbf{d}}_2$, and $\hat{\mathbf{d}}_3$, respectively, and that there is no slip between the omniwheels and the spherical magnet. Given a magnet angular velocity $\boldsymbol{\omega}_{\mathbf{m}}$, the surface velocity of the magnet at the i^{th} omniwheel-magnet contact point is

$$\mathbf{u}_i = r_m \boldsymbol{\omega}_{\mathbf{m}} \times \hat{\mathbf{d}}_i, \quad (2.1)$$

where r_m is the radius of the spherical magnet.

The components of \mathbf{u}_1 , \mathbf{u}_2 , and \mathbf{u}_3 parallel to the respective omniwheel axes are transferred directly into rotation of the omniwheel rollers and cause no rotation of the omniwheels themselves. All other components of \mathbf{u}_1 , \mathbf{u}_2 , and \mathbf{u}_3 cause each omniwheel to rotate with scalar rotation speeds ω_{a1} , ω_{a2} , and ω_{a3} , respectively. The component direction of \mathbf{u}_i that causes the i^{th} omniwheel to rotate about its axis is

$$\hat{\mathbf{q}}_i = \hat{\mathbf{d}}_i \times \hat{\mathbf{a}}_i. \quad (2.2)$$

Under the assumption of no-slip, the projection of \mathbf{u}_1 , \mathbf{u}_2 , and \mathbf{u}_3 onto the directions $\hat{\mathbf{q}}_1$, $\hat{\mathbf{q}}_2$, and $\hat{\mathbf{q}}_3$, respectively, must be mapped to the scalar rotation speeds of each omniwheel by the reciprocal of the omniwheels' radii (denoted by the constant r_w , as identical omniwheels are assumed throughout this thesis) as

$$\omega_{ai} = \frac{1}{r_w} \hat{\mathbf{q}}_i^T \mathbf{u}_i = \frac{r_m}{r_w} \hat{\mathbf{a}}_i^T \{\hat{\mathbf{d}}_i\}^2 \boldsymbol{\omega}_m, \quad (2.3)$$

where $\{\hat{\mathbf{d}}_i\} \in \text{so}(3)$ is a skew-symmetric matrix form of the cross-product operation defined by

$$\{\zeta\} = \begin{bmatrix} 0 & -\zeta_3 & \zeta_2 \\ \zeta_3 & 0 & -\zeta_1 \\ -\zeta_2 & \zeta_1 & 0 \end{bmatrix}. \quad (2.4)$$

All three omniwheel scalar rotation speeds can be packed into the vector $\boldsymbol{\omega}_a$ and related to the spherical magnet angular velocity $\boldsymbol{\omega}_m$ in matrix form as

$$\boldsymbol{\omega}_a = \begin{bmatrix} \omega_{a1} \\ \omega_{a2} \\ \omega_{a3} \end{bmatrix} = \frac{r_m}{r_w} \begin{bmatrix} \hat{\mathbf{a}}_1^T \{\hat{\mathbf{d}}_1\}^2 \\ \hat{\mathbf{a}}_2^T \{\hat{\mathbf{d}}_2\}^2 \\ \hat{\mathbf{a}}_3^T \{\hat{\mathbf{d}}_3\}^2 \end{bmatrix} \boldsymbol{\omega}_m. \quad (2.5)$$

Due to the assumption that $\hat{\mathbf{a}}_i$ is perpendicular to $\hat{\mathbf{d}}_i$, (2.5) can be simplified to

$$\boldsymbol{\omega}_a = \frac{r_m}{r_w} \begin{bmatrix} -\hat{\mathbf{a}}_1^T \\ -\hat{\mathbf{a}}_2^T \\ -\hat{\mathbf{a}}_3^T \end{bmatrix} \boldsymbol{\omega}_m = \eta \mathbf{A}^T \boldsymbol{\omega}_m, \quad (2.6)$$

where $\eta = -r_m/r_w$ is the gear ratio from the omniwheels to the sphere (with the negative sign indicating the change in rotation direction from the omniwheels to the magnet), and the matrix \mathbf{A} is defined as

$$\mathbf{A} = [\hat{\mathbf{a}}_1 \quad \hat{\mathbf{a}}_2 \quad \hat{\mathbf{a}}_3]. \quad (2.7)$$

The omniwheel axes and positioning must be designed such that the matrix \mathbf{A} has full rank; otherwise there will exist a direction of $\boldsymbol{\omega}_m$ that cannot be achieved with any selection of omniwheel rotation speeds. Although linear independence of the columns of

\mathbf{A} is a sufficient condition mathematically, in practice the columns should be designed to be as close to mutually orthogonal as possible. Otherwise, some desired $\boldsymbol{\omega}_{\mathbf{m}}$ will require an unnecessarily, and possibly unachievably, large omniwheel rotation speed. Figure 2.1 shows three possible arrangements of omniwheels that are arranged so that the columns of \mathbf{A} are mutually orthogonal; image (c) shows the configuration utilized in previous ballbot designs [19–22].

Throughout this thesis it is assumed that \mathbf{A} is always invertible, which is equivalent to $\hat{\mathbf{a}}_1, \hat{\mathbf{a}}_2$, and $\hat{\mathbf{a}}_3$ being linearly independent. Similar to how angular velocity is mapped from magnet-space to motor-space through \mathbf{A}^\top , torque is similarly transmitted, but with the inverse of the gear ratio:

$$\boldsymbol{\tau}_{\mathbf{a}} = \frac{1}{\eta} \mathbf{A}^\top \boldsymbol{\tau}_{\mathbf{m}}. \quad (2.8)$$

It is possible to violate the assumption that each vector $\hat{\mathbf{d}}_i$ from the spherical magnet’s center to the contact point of the i^{th} omniwheel is perpendicular to the i^{th} omniwheel axis $\hat{\mathbf{a}}_i$ and reformulate the device kinematics more generally. However, this would require an entirely different style of omniwheel to ensure that contact is continuously maintained throughout each omniwheel revolution.

2.2 Detecting the Magnet’s Dipole Moment

The dipole moment of the magnetic body (denoted by the vector \mathbf{m}) is the vector from the south to north poles of the magnet (see Fig. 2.2). Methods of magnetic manipulation using a single permanent magnet require the magnet’s dipole moment to be specifically directed and require the dipole moment to be known [14–16]. The dipole moment \mathbf{m} of the SAMM’s magnet can be determined by measuring the magnetic field \mathbf{h} that it generates in space.

One approach to measuring the magnetic field uses Hall-effect sensors. Hall-effect sensors measure the component of the field in the direction normal to (i.e., passing through) the sensor’s face. We assume the general case of n Hall-effect sensors. Let each sensor be positioned in space such that the vectors \mathbf{p}_1 through \mathbf{p}_n , in units of meters, measure each sensor’s position relative to the spherical magnet’s center, and let $\hat{\mathbf{v}}_1$ through $\hat{\mathbf{v}}_n$ be unit-magnitude vectors that describe the directions that are sensed by each sensor; all vectors are expressed in the same frame as \mathbf{m} (see Fig. 2.2). Let the magnetic field at each sensor position be denoted by \mathbf{h}_1 through \mathbf{h}_n , in units $\text{A} \cdot \text{m}^{-1}$. The measured component of the field produced by the i^{th} sensor is denoted with the scalar s_i and is given by

$$s_i = \hat{\mathbf{v}}_i^\top \mathbf{h}_i. \quad (2.9)$$

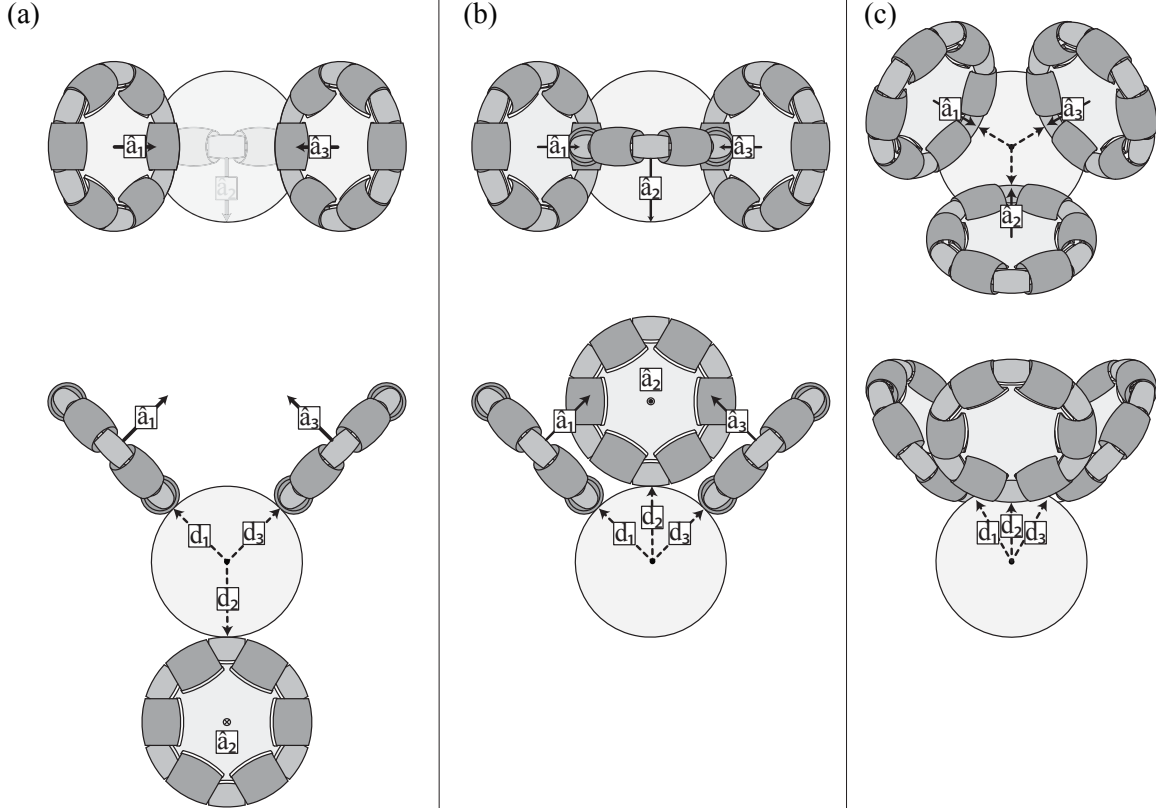


Figure 2.1. Three potential omniwheel configurations. In each configuration, the axis of each omniwheel is orthogonal to the contact-point vector of the omniwheel and the spherical magnet ($\hat{\mathbf{d}}_1$, $\hat{\mathbf{d}}_2$, and $\hat{\mathbf{d}}_3$), and all three omniwheel axes ($\hat{\mathbf{a}}_1$, $\hat{\mathbf{a}}_2$, and $\hat{\mathbf{a}}_3$) are mutually orthogonal.

The magnetic field \mathbf{h}_i , at each sensor position \mathbf{p}_i , can be predicted with the point-dipole model

$$\mathbf{h}_i = \frac{1}{4\pi \|\mathbf{p}_i\|^3} \left(3\hat{\mathbf{p}}_i\hat{\mathbf{p}}_i^\top - \mathbf{I}_3 \right) \mathbf{m} = \mathbf{H}_i \mathbf{m}, \quad (2.10)$$

where $\mathbf{I}_3 \in \mathbb{R}^{3 \times 3}$ is the identity matrix. Equation (2.10) exactly predicts the field produced by a spherical permanent magnet. For all other geometries, it is an approximation that becomes more accurate with increasing distance [25, 26].

Substituting (2.10) into (2.9) produces an expression relating the magnet's dipole moment \mathbf{m} to each of the n sensor measurements, which can be aggregated into the matrix equation

$$\mathbf{s} = \begin{bmatrix} s_1 \\ \vdots \\ s_n \end{bmatrix} = \begin{bmatrix} \hat{\mathbf{v}}_1^\top \mathbf{H}_1 \\ \vdots \\ \hat{\mathbf{v}}_n^\top \mathbf{H}_n \end{bmatrix} \mathbf{m} = \mathbf{S} \mathbf{m}. \quad (2.11)$$

The $n \times 3$ constant matrix \mathbf{S} encapsulates the complete geometric description of the sensor arrangement, as it pertains to estimating \mathbf{m} . If the matrix \mathbf{S} has full column rank, then a

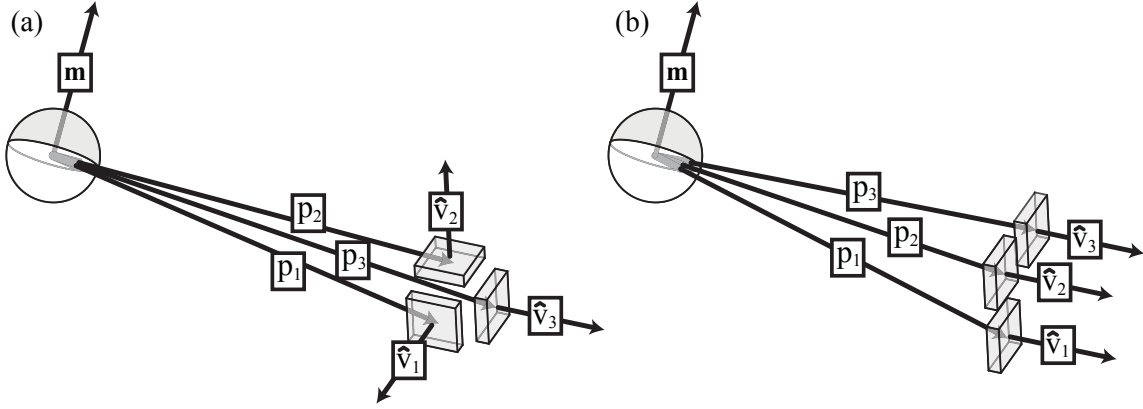


Figure 2.2. Two potential arrangements of Hall-effect sensors that can be used to measure the direction of the magnetic body's dipole moment \mathbf{m} . In configuration (a), the three sensors measure the magnetic field in mutually orthogonal directions. If $\mathbf{p}_1 \approx \mathbf{p}_2 \approx \mathbf{p}_3$, then the dipole moment \mathbf{m} can be found by inverting the point-dipole model (2.10) using the field measured by the sensors. In configuration (b), the three sensors measure the magnetic field in the same direction but at different positions.

solution for the dipole moment \mathbf{m} can be found as

$$\mathbf{m} = \mathbf{S}^\dagger \mathbf{s}, \quad (2.12)$$

where $\mathbf{S}^\dagger = \mathbf{V}\mathbf{\Sigma}^\dagger\mathbf{U}^\top$ is the Moore-Penrose pseudoinverse of \mathbf{S} , using the singular-value decomposition $\mathbf{S} = \mathbf{U}\mathbf{\Sigma}\mathbf{V}^\top$, where the columns of \mathbf{U} and \mathbf{V} are the output and input singular vectors of \mathbf{S} , respectively, $\mathbf{\Sigma}$ contains the singular values of \mathbf{S} on the main diagonal and zeros elsewhere, and $\mathbf{\Sigma}^\dagger$ is the transpose of $\mathbf{\Sigma}$ in which the nonzero singular values have been replaced by their reciprocals [27]. The matrix \mathbf{S} should be made to have full column rank by using at least three Hall-effect sensors and appropriately selecting the positions (\mathbf{p}_i) and directions ($\hat{\mathbf{v}}_i$) of each sensor. When $n > 3$, (2.12) provides the best estimate of \mathbf{m} in a least-squares sense. The constant matrix \mathbf{S}^\dagger can be calculated off-line.

The vector of sensor measurements \mathbf{s} can be modeled as a normal multivariate random process $\mathbf{s} \sim \mathcal{N}(\boldsymbol{\mu}, \mathbf{P})$ with mean vector $\boldsymbol{\mu} \in \mathbb{R}^n$ and covariance matrix $\mathbf{P} \in \mathbb{R}^{n \times n}$. The sensor measurement distribution \mathbf{s} is propagated through (2.12) to a normal multivariate random process of the measured dipole moment

$$\mathbf{m} \sim \mathcal{N}\left(\mathbf{S}^\dagger \boldsymbol{\mu}, \mathbf{S}^\dagger \mathbf{P} (\mathbf{S}^\dagger)^\top\right). \quad (2.13)$$

Under the assumption that the sensor measurements are independent with the same variance ρ^2 , which is a reasonably accurate assumption for batch-fabricated sensors, the

covariance matrix can be expressed as $\mathbf{P} = \rho^2 \mathbf{I}_n$, which simplifies the distribution of the measured dipole moment to

$$\mathbf{m} \sim \mathcal{N}(\mathbf{S}^\dagger \boldsymbol{\mu}, \rho^2 \mathbf{V} (\boldsymbol{\Lambda}^{-1})^2 \mathbf{V}^\top). \quad (2.14)$$

where $\boldsymbol{\Lambda}$ is the 3×3 diagonal submatrix of $\boldsymbol{\Sigma}$ with the singular values of \mathbf{S} on its diagonal. Along with making \mathbf{S} full rank, the sensors should also be ideally arranged to minimize the variance of the measured dipole moment by decreasing the singular values of the dipole moment covariance (stored on the diagonal of $\boldsymbol{\Lambda}^{-1}$), which is equivalent to maximizing the singular values of \mathbf{S} . This simplifying formulation can be useful in the design of the sensor placement. However, during runtime, the formulation in (2.13) allows us to account for differences in variance between sensors.

Figure 2.2 shows two example arrangements of three Hall-effect sensors. In the configuration of Fig. 2.2(a), all three sensors are mutually orthogonal. If \mathbf{p}_1 , \mathbf{p}_2 , and \mathbf{p}_3 are nearly the same (i.e., the sensors are approximately collocated), then the sensors effectively measure the magnetic field vector \mathbf{h} at their common position, and \mathbf{m} can be found by inverting the point-dipole model (2.10), which is always invertible and well-conditioned. In the configuration of Fig. 2.2(b), each sensor faces the same direction. In this arrangement, the matrix \mathbf{S} becomes rank-deficient when the sensors become collocated, implying that sensors measuring the same direction should be located in distinct positions.

Although (2.12) can provide an instantaneous reading of the magnet's measured dipole, in practice a Kalman filter is employed to incorporate the manipulator's dynamics with the sensor readings to reduce noise in the system. Details providing the derivation and implementation of the Kalman filter are discussed in Chapters 4 and 6.

CHAPTER 3

PROTOTYPE IMPLEMENTATION

The field produced by the spherical magnet, which is accurately modeled by the point-dipole model (2.10), is very strong in close proximity. As a result, great care must be taken during the design of components that contact or are near the spherical magnet, as they may experience strong magnetic fields. For example, any soft-magnetic SAMM component near the spherical magnet will become magnetized and can exert a magnetic torque and force on the spherical magnet that may hinder its free rotation, potentially resulting in the loss of control authority. Additionally, time-varying magnetic fields (caused by rotating the spherical magnet) induce eddy currents (also known as Foucault currents) in nearby electrically conductive material; these circulating currents create their own magnetic field, resulting in magnetic drag on the spherical magnet. Our prototype instantiation is constructed with nonmagnetic components that mitigate disturbances from soft-magnetic materials, and components near the spherical magnet are constructed from electrically nonconductive materials to mitigate disturbances from eddy currents, with the exception of the gearmotors, which are intentionally positioned far from the spherical magnet.

Our prototype instantiation of the SAMM described herein is shown in Fig.3.1. The magnetic body is a 50.8-mm-diameter, Grade-N42, spherical permanent magnet with a dipole strength of $71.6 \text{ A} \cdot \text{m}^2$.

The form-closure constraints that allow only rotation of the spherical magnet are implemented with a set of four ball-roller-tipped precision set screws. The smallest number of such constraints needed to guarantee form-closure is four, with three constraints whose contact points on the magnet do not form a hemispherical great circle on the actuator magnet and a fourth constraint contacting normal to the plane established by the first three. Housed inside the tip of the set-screw is a freely rotating 5.56-mm ball that is supported by 1.50-mm subrollers. The set-screws are threaded into the housing of the mechanism so that they constrain the magnet in its desired position with minimal perceptible play when installed flush with reference bosses on the exterior of the housing. The body of the

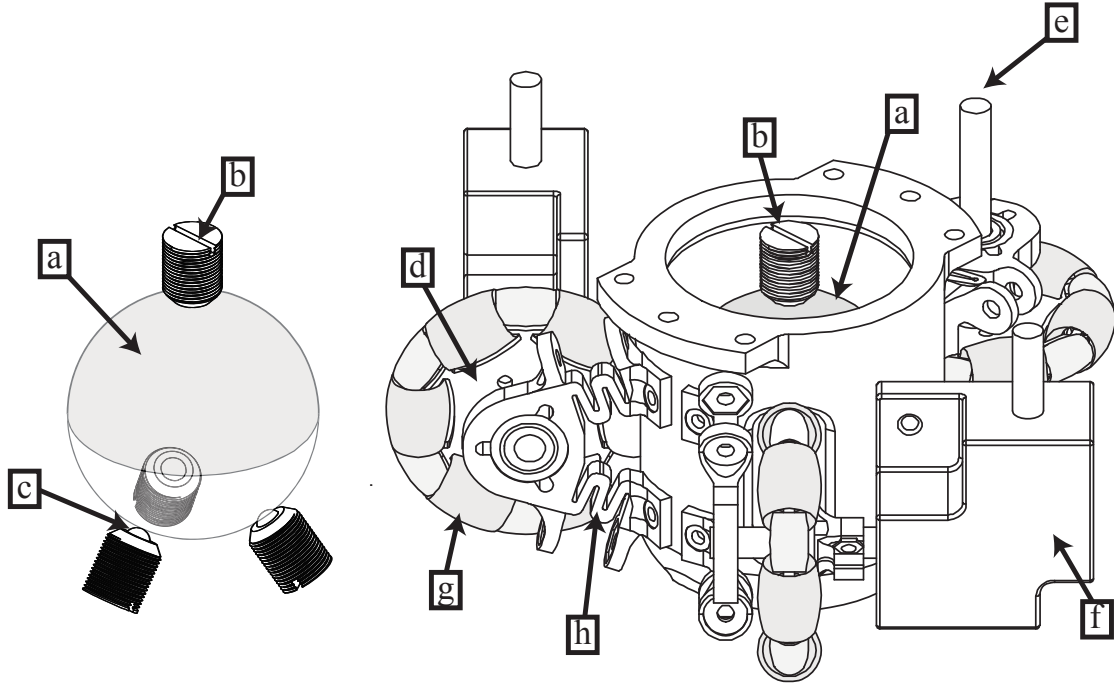


Figure 3.1. An instantiation of the SAMM described herein. The spherical magnet (a) is supported by an arrangement of set-screws (b), each containing a ball-roller tip (c). The spherical magnet is driven by three orthogonal omniwheels (d), which are in-turn driven by parallel driveshafts (e) due to the application of 90° gearboxes (f) for two of the omniwheels. To improve driving traction, the omniwheel rollers are coated in a soft neoprene layer (g) and are tensioned onto the spherical magnet with adjustable compliant pillow blocks (h).

set-screws are nylon, and the ball-tip and subrollers are ceramic, making each set-screw nonmagnetic and nonconductive.

The housing of the device resembles a cylindrical structure with a hemisphere at one end where three of the four form-closure constraints are mounted. The housing is constructed out of nonconductive ABS plastic to mitigate eddy currents. The omniwheels contact the magnet through windows in the cylindrical body and are arranged in the counteropposed configuration of Fig. 2.1(a). This configuration allows the normal forces from one omniwheel to be transmitted to the other omniwheels, which mutually increases their traction. Unlike the other two configurations shown in Fig. 2.1, the normal forces applied by the counteropposed omniwheels are not carried by the form-closure constraints, resulting in lower rotating friction. This counteropposed configuration yields the omniwheel axes:

$$\begin{aligned}\hat{\mathbf{a}}_1 &= [\sqrt{2}/2 \quad \sqrt{2}/2 \quad 0]^\top \\ \hat{\mathbf{a}}_2 &= [0 \quad 0 \quad -1]^\top \\ \hat{\mathbf{a}}_3 &= [\sqrt{2}/2 \quad -\sqrt{2}/2 \quad 0]^\top.\end{aligned}$$

The omniwheels are driven by three Maxon RE-max 29 gearmotors (Part No. 454219), which have a 24:1 gear ratio and 512 CPT magnetic encoders, mounted in a parallel arrangement (Fig. 3.2). The torques applied to omniwheel axes $\hat{\mathbf{a}}_1$ and $\hat{\mathbf{a}}_3$ are redirected via 90° gearboxes; the torque applied to omniwheel axis $\hat{\mathbf{a}}_2$ is transmitted via direct-drive. The 90° gearboxes consist of nylon gears mounted to aluminum shafts and are supported by dual acetal ball bearings inside an aluminum case, making the 90° gearboxes entirely nonmagnetic. The gearmotors are connected to the gearboxes and the omniwheel drive shaft (in the case of axis $\hat{\mathbf{a}}_2$) by aluminum helical couplings.

3.1 Omniwheels

The omniwheels developed and employed on the SAMM are miniature continuous omniwheels based on [19, 23, 24], which provide nearly continuous contact with the magnet. Each omniwheel roller contains dual ceramic ball bearings for minimal friction under load, as well as a soft neoprene heat-shrink sleeve on the surface for increased traction. Unlike the omniwheels used in [19, 23, 24], the omniwheels employed on the SAMM have no axles and the hub is constructed out of one piece—a simplifying innovation that has enabled us to construct smaller-scale omniwheels than in [19, 23, 24]. Due to the omniwheels’ proximity to the spherical magnet, the omniwheels have been constructed with fully nonmagnetic components. Some of the omniwheel components are conductive, but their volume is small and they are sufficiently far from the spherical magnet so that effects from eddy currents are not noticeable. When fully assembled, the major diameter of each omniwheel is 58.2 mm.

Each omniwheel is assembled from components illustrated in Fig. 3.3. Assembly begins with a high-strength 7075 aluminum hub, which is waterjet cut out of a 2.286-mm-thick (0.090 in) sheet of material. Rectangular-cross-sectioned spindles (that replace the functionality of a more traditional axle) are cut into the profile of the hub (Fig. 3.3(a)). Ceramic MR63 ball bearings are bonded onto each spindle (Fig. 3.3(b)) using *Krazy Glue*® adhesive; the adhesive both secures the ceramic bearings in position and alleviates point-contact stresses resulting from the interface of the spindles’ rectangular cross-section and the bearings’ circular bore. An omniwheel contains small and large 3D-printed plastic rollers that

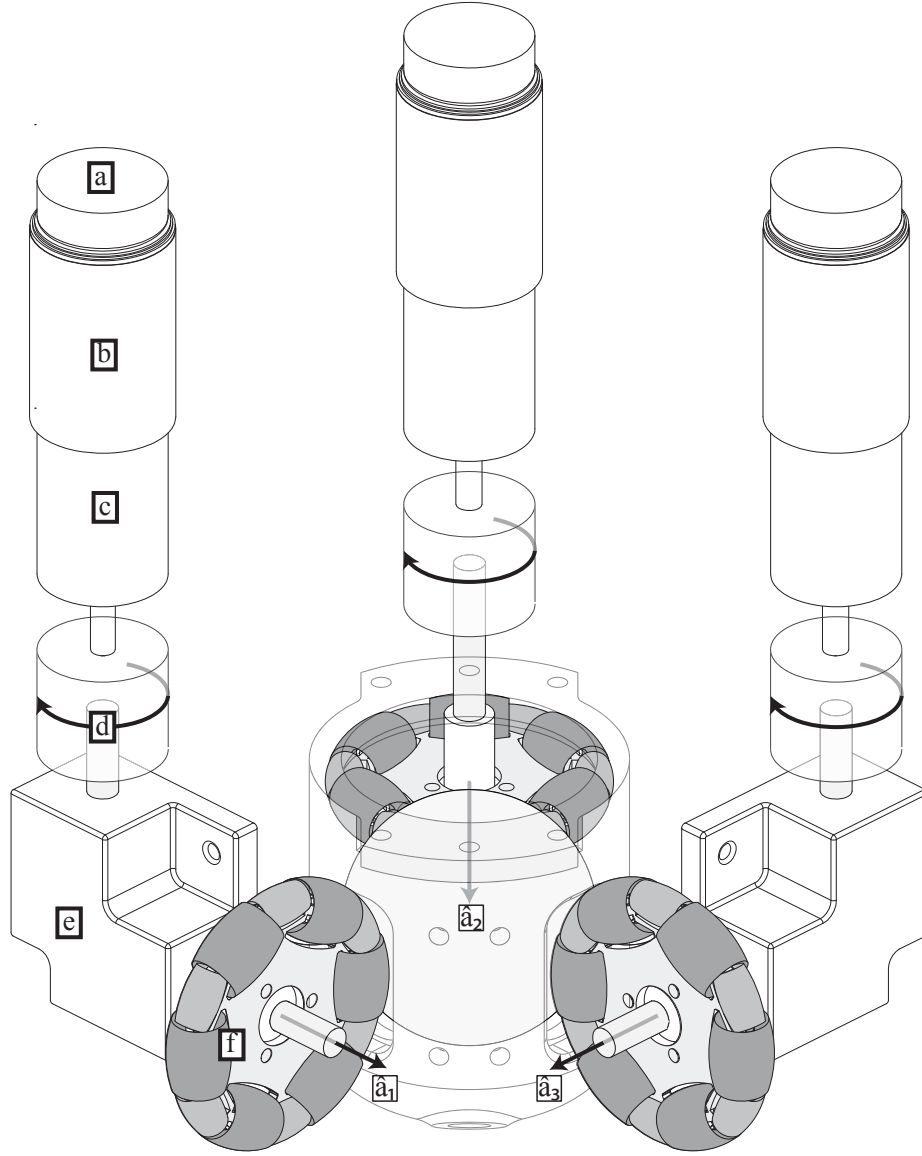


Figure 3.2. A parallel arrangement of gearmotors, each consisting of an encoder (a), a DC-motor (b), and a gearhead (c), which transmit torque to the mutually orthogonal omniwheel axes \hat{a}_i through helical couplings (d). Two of the axes utilize 90° gearboxes (e). Omniwheels (f) contact the spherical magnet through openings in the housing.

measure 7.97 mm and 13.00 mm at their largest diameters and 12.5 mm and 15.7 mm in length, respectively (Figs. 3.3(b) and 3.3(c)). The rollers are printed in halves, which are assembled around the bearings using pockets in the rollers' interior that accommodate the ball-bearings' cylindrical geometry as portrayed in Figs. 3.3(b) and 3.3(c).

The rollers are secured together by an outer layer of soft neoprene heat-shrink tubing, which is adhered to the rollers' exterior to prevent the neoprene from sliding using *Gorilla Glue*[®] adhesive. The rollers are assembled with the neoprene by placing the unshrunk

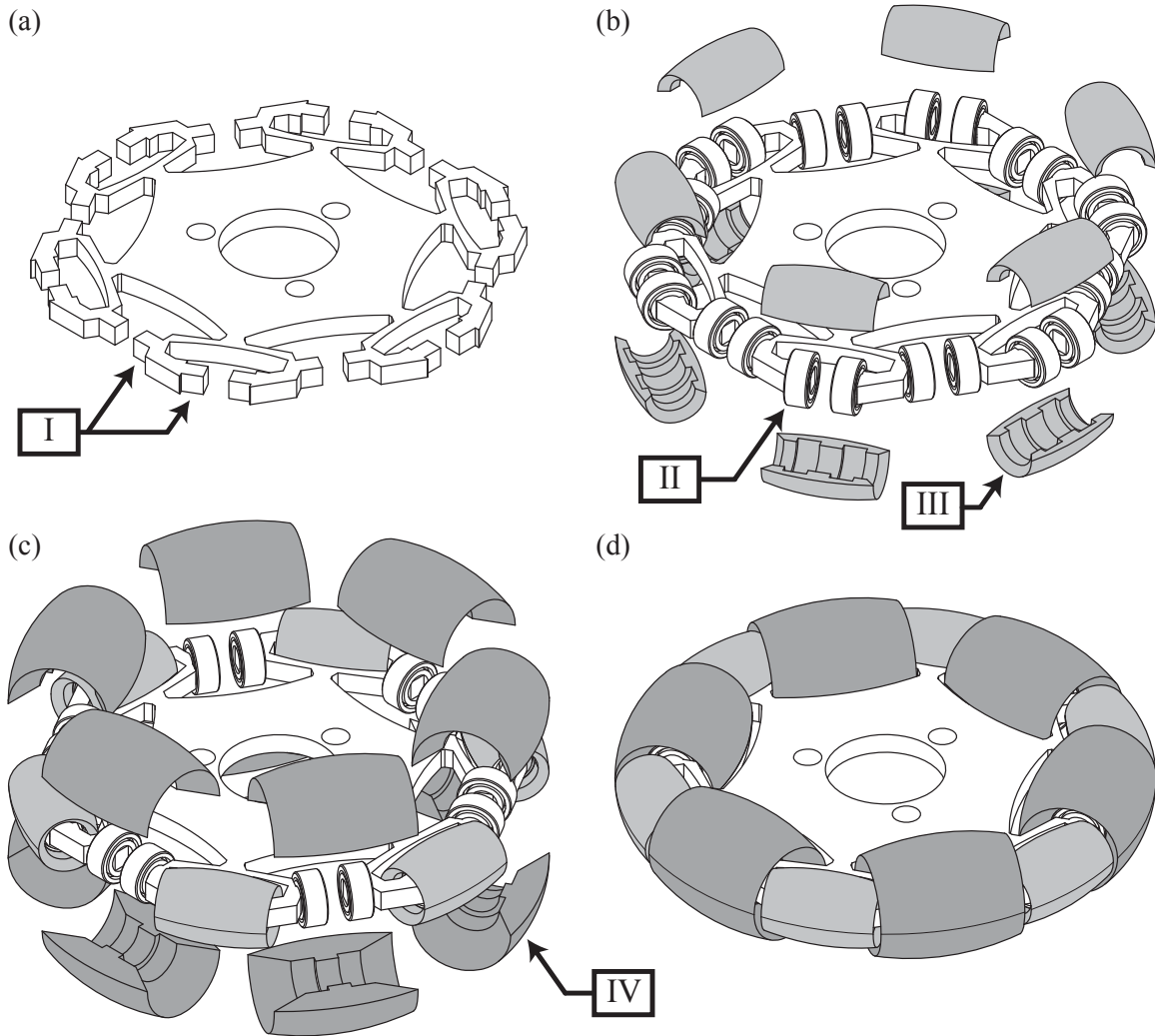


Figure 3.3. Assembly process of the omniwheels used on the SAMM. (a) The omniwheel hubs are waterjet cut from high-strength 7075 aluminum and incorporate spindles (I) that replace the functionality of axles. (b) Ceramic MR63 ball-bearings (II) are bonded onto the spindles, and the plastic small-roller halves (III) are assembled around the bearings. Neoprene sleeves (not shown) are adhered to the small-rollers' exterior. (c) Finally, the large-roller halves (IV) are installed and neoprene sleeves (not shown) are bonded to their exterior. The completed omniwheel assembly is shown (d).

tubing into position on the omniwheel and then placing the roller halves onto the bearings through the empty space available inside the unshrunk tubing. *Gorilla Glue*[®] adhesive is applied to the rollers' exterior, hot air is used to shrink the tubing, and any excess tubing material is trimmed off. Note that the roller halves are not bonded together. Rather, the adhesive applied to the rollers' exterior keeps the neoprene tubing from sliding, and the compression from the tubing keeps the roller halves together. When fully assembled, the omniwheel's rollers pose little discernible rolling resistance in their passive directions while

retaining traction in their driving direction.

3.2 Compliance for Magnet and Omniwheel Irregularities

Irregularities exist in the omniwheels' circularity caused by gaps/steps between omni-wheel rollers, unintentional eccentricity in the mechanical mounting, etc. Designing passive compliance into the omniwheel-drive mechanism that allows the omniwheels' motion to compensate for irregularities can keep the omniwheels robustly in contact with the spherical magnet.

Ideally, the built-in compliance should allow compensation for omniwheel irregularities without altering the torque transmission matrix \mathbf{A} . Any mechanism that keeps $\hat{\mathbf{a}}_i$ constant and maintains $\hat{\mathbf{a}}_i$ perpendicular to $\hat{\mathbf{d}}_i$ through its range of travel will satisfy this condition. Mechanisms that satisfy this requirement could include straight-line mechanisms such as the Hart's Inversor, Sarrus linkage, or other more general space-crank mechanisms that allow the omniwheel to move in the $\hat{\mathbf{d}}_i$ direction [28]. A simple 1-DOF rotary joint can be designed that keeps the \mathbf{A} matrix constant (Fig. 3.4(a)). Another type of mechanism could exploit the potential-energy well created by spring-loaded pillow blocks that approximate linear motion (Fig. 3.4(b)). Note that spring-loaded pillow blocks can allow small changes in the direction of $\hat{\mathbf{a}}_i$, keeping \mathbf{A} only *approximately* constant.

The instantiation of the SAMM shown here employs two of the aforementioned approaches: 1-DOF rotary motion is employed on the 1st and 3rd omniwheels as illustrated Fig. 3.4(a), and approximate straight-line motion of the 2nd omniwheel is achieved with two compliant pillow blocks as illustrated in Fig. 3.4(b). In the rotary case, both rotary axes lie parallel to the respective omniwheel axes (i.e., $\hat{\mathbf{a}}_1$ in the case of the 1st omniwheel and $\hat{\mathbf{a}}_3$ in the case of the 3rd omniwheel). The 90° gearboxes make the rotary axis perpendicular to the respective motor axis, which decouples the direction of compliance from the direction of motor torque transmission. If the direction of compliance were not decoupled from the motor-torque direction of transmission, then both omniwheel irregularities and torque transmission would cause the tensioning mechanisms to move in the direction of compliance, which could result in increased friction or traction loss. Tension is applied to the 1st and 3rd omniwheel assemblies by adjustable spring-tensioned pillow blocks. The pillow blocks are constructed of 3D-printed ABS plastic with cutouts revealing serpentine shaped springs (visible in Fig. 3.4). The serpentine spring is reinforced with a silicone compression spring whose tension can be increased or decreased by tightening or loosening an adjustment screw.

On the 2nd omniwheel, approximate straight-line motion is formed utilizing two ad-

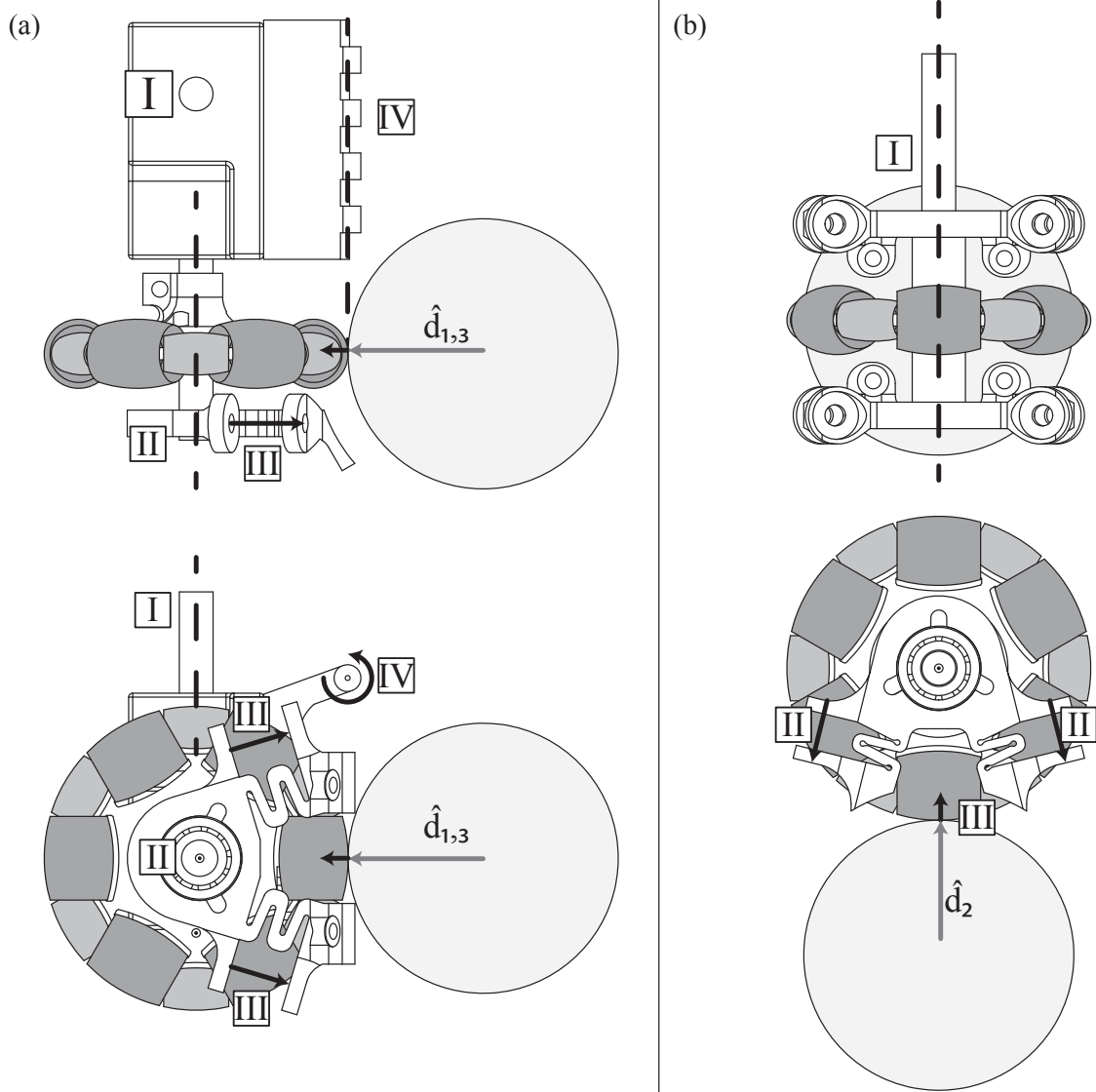


Figure 3.4. Motion in each of the omniwheel axes \hat{a}_i is shown. Planar-rotary motion in the 1st and 3rd omniwheels is illustrated (a), where the motor's axis (I) is transmitted through the 90° gearbox to the omniwheel axes (II). Adjustable spring-tensioned pillow blocks provide force (III) between the omniwheel and the spherical magnet, allowing for compliance (IV) locally parallel with \hat{d}_i . Translational motion in the 2nd omniwheel is shown in (b), where the motor axis and the omniwheel axis are coaxial (I). Adjustable spring-tensioned pillow blocks provide force (II) between the omniwheel and the spherical magnet, allowing for compliance (III) parallel with \hat{d}_2 .

justable spring-tensioned pillow blocks, similar to those used on the 1st and 3rd axes, to tension the omniwheel directly onto the spherical magnet in the direction $\hat{\mathbf{d}}_2$, illustrated in Fig. 3.4(b). Although the motion is not strictly constrained to $\hat{\mathbf{d}}_2$, we have found that the deviation is small and results in insignificant changes to the \mathbf{A} matrix.

3.3 Hall-Effect Sensor Cluster

A sensor cluster, consisting of six 1-DOF Allegro A1302 Hall-effect sensors arranged on the surface of a cube and positioned in close proximity to each other, is mounted to the housing as shown in Fig. 3.5 and described quantitatively in Table 3.1. In addition to being a space free from moving parts, this location ensures that magnetic-field disturbances in the workspace below the SAMM (e.g., from the magnet of a device being manipulated by the SAMM) have a minimal impact on the estimation of the actuating magnet's dipole heading. The gearmotors are the nearest magnetic component to the sensor cluster, but they are positioned sufficiently far away to make their contribution to the measured magnetic field negligible. The sensors are chosen with a sensitivity of 13 mV/mT (1.3 mV/G), which utilizes their full output-voltage range without saturation. Future instantiations could implement a wider array of Hall-effect sensors in place of the existing cluster.

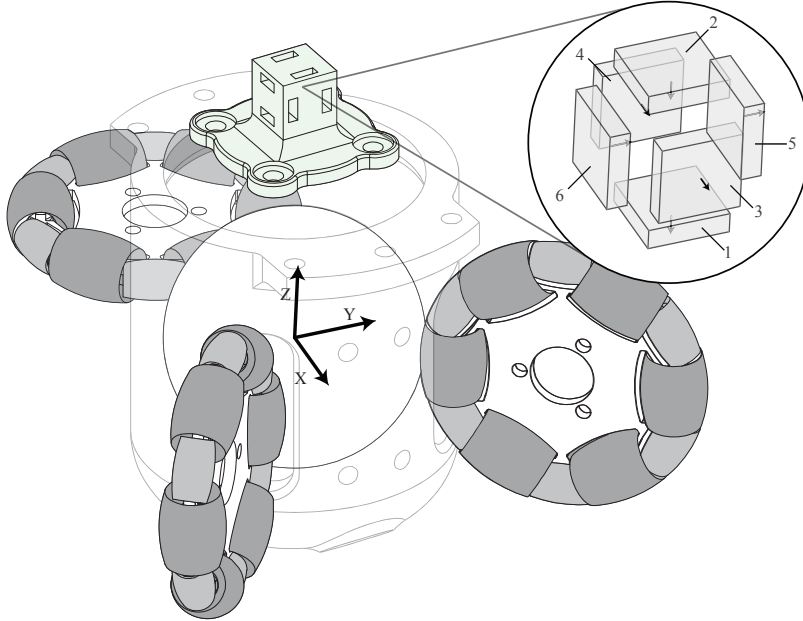


Figure 3.5. A sensor cluster containing six 1-DOF Hall-effect sensors is mounted directly above the housing. The coordinate system and numbering system used is shown.

Table 3.1. Parameters of Hall-effect sensor cluster used on the prototype SAMM are shown. The vector from the magnet to the i^{th} sensor (\mathbf{p}_i) and its respective sensing direction (\mathbf{v}_i) are shown.

Hall-Effect Sensor	Position Vector (mm) \mathbf{p}_i^T	Sensing Direction \mathbf{v}_i^T
1	[0, 0, 51.0]	[0,0,1]
2	[0, 0, 58.5]	[0,0,1]
3	[3.75, 0, 54.7]	[1,0,0]
4	[-3.75, 0, 54.7]	[1,0,0]
5	[0, 3.75, 54.7]	[0,1,0]
6	[0, -3.75, 54.7]	[0,1,0]

3.4 System Integration

The complete device (rendering shown in Fig. 3.6, and prototype shown in Fig. 3.7) is intended to be mounted to a structure by a mounting platform, where additional mounting hardware for the gearmotors is also attached. The entire assembly may be mounted as the end-effector of a multi-DOF robotic manipulator (e.g., as in Fig. 3.7) or as a stand-alone manipulator. In either case, the SAMM will add three orientation DOF to the existing structure. In the case of a 3-DOF Cartesian robot, for example, the device will enable 6-DOF holonomic dipole control. In this configuration the prototype device can be positioned so that the device “bottom” (the hemispherical side where three of the four set-screws are located), which is streamlined and free of moving parts, is presented to the manipulation workspace, reducing the risk of damage to the moving SAMM components and enabling the spherical actuator magnet to be positioned close to the remote magnetic device being manipulated.

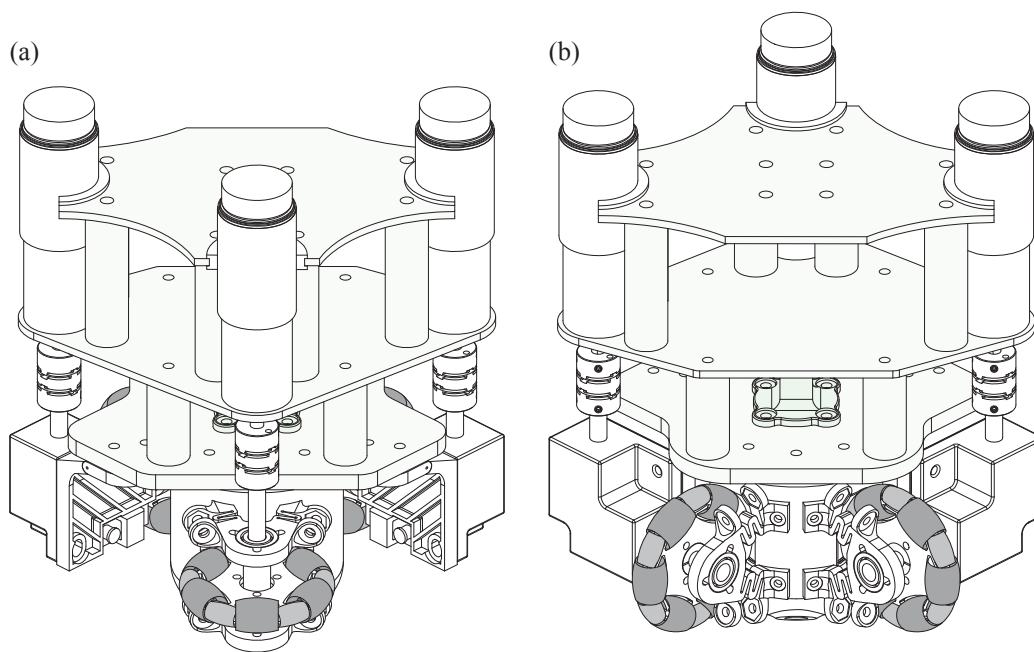


Figure 3.6. Rendering of the SAMM with necessary mounting hardware, complete with gearmotor mounts and mounting platform.



Figure 3.7. Prototype SAMM shown mounted to the tool frame (a) of robotic manipulator. Encoders (b) measure the gearmotors' (c) position. The cluster of Hall-effect sensors (d) measures the spherical magnet's dipole. Power is transmitted through aluminum helical shaft couplings (e) to omniwheel axles or 90° gearboxes (g), which pivot for omniwheel compliance (f). Omniwheels (h) are tensioned to the spherical magnet through adjustable spring-tensioned pillow blocks (i), whose tension can be manually tuned through adjustment screws (j).

CHAPTER 4

STATE ESTIMATION

In applications where sensory data are imprecise, due to noise or other inaccuracies, a Kalman filter can be employed to produce better estimates of state information. In the case where the state transition model is nonlinear (as is the case with heading control of a rotating dipole), the Extended Kalman Filter should be employed. The Extended Kalman Filter is the nonlinear extension to the Kalman Filter, which linearizes the system's dynamic and observation equations about the current predicted state before employing the Kalman Filter algorithm [29]. We have chosen to implement the Hybrid Extended Kalman Filter [30], which uses continuous-time differential equations for modeling the system's dynamics and performs system observation in discrete time.

4.1 Review of the Hybrid Extended Kalman Filter

The derivation described in Section 4.1 is taken from [30]. The hybrid implementation (otherwise known as the discrete-time implementation) allows for the state $\mathbf{x}(t)$ to transition continuously according to the model

$$\dot{\mathbf{x}}(t) = \mathbf{f}(\mathbf{x}(t), \mathbf{u}(t)) + \mathbf{w}(t), \quad (4.1)$$

where $\mathbf{f}(\mathbf{x}(t), \mathbf{u}(t))$ models the system's dynamics given the input $\mathbf{u}(t)$ and process noise $\mathbf{w}(t) \sim \mathcal{N}(0, \mathbf{Q})$. The continuous model (4.1) is used to create a discrete-time state transition model of the form:

$$\mathbf{x}_j = \mathbf{x}_{j-1} + \int_{t_{j-1}}^{t_j} \dot{\mathbf{x}}(t) dt, \quad (4.2)$$

where t_j is the time at the j^{th} step and $\mathbf{x}_j = \mathbf{x}(t_j)$. The measurement model is given by

$$\mathbf{z}_j = \mathbf{h}(\mathbf{x}_j) + \mathbf{v}_j, \quad (4.3)$$

where $\mathbf{v}_j \sim \mathcal{N}(0, \mathbf{R})$ is the measurement noise.

The estimator is initialized with an initial estimate of the state $\bar{\mathbf{x}}(t_0)$ and an initial covariance of the state estimate $\mathbf{P}(t_0)$.

$$\bar{\mathbf{x}}_0 = \bar{\mathbf{x}}(t_0) = \mathbb{E}[\mathbf{x}(0)] \quad (4.4)$$

$$\mathbf{P}_0 = \mathbf{P}(t_0) = \text{Var}[\mathbf{x}(0)] \quad (4.5)$$

4.1.1 Predict

An apriori state estimate can be predicted with (4.2) using a zero-order hold on the system inputs $\mathbf{u}(t)$:

$$\mathbf{x}_{j|j-1} = \mathbf{x}_{j-1|j-1} + \int_{t_{j-1}}^{t_j} \mathbf{f}(\mathbf{x}(t), \mathbf{u}(t_{j-1})) dt. \quad (4.6)$$

Similarly to the state estimate, the a priori state-covariance estimate is predicted by integrating the continuous-time derivative of the state covariance:

$$\mathbf{P}_{j|j-1} = \mathbf{P}_{j-1|j-1} + \int_{t_{j-1}}^{t_j} \dot{\mathbf{P}}(t) dt. \quad (4.7)$$

The derivative of the state covariance $\dot{\mathbf{P}}(t)$ can be determined using the current state covariance $\mathbf{P}_{j-1} = \mathbf{P}(t_{j-1})$, the linearization $\mathbf{F}(t)$ of the state-transition model $\mathbf{f}(t)$, and the covariance of the process noise \mathbf{Q} :

$$\dot{\mathbf{P}}(t) = \mathbf{F}(t)\mathbf{P}(t) + \mathbf{P}(t)\mathbf{F}(t)^\top + \mathbf{Q}, \quad (4.8)$$

where

$$\mathbf{F}(t) = \left. \frac{\partial \mathbf{f}}{\partial \mathbf{x}} \right|_{\bar{\mathbf{x}}(t), \mathbf{u}(t)}. \quad (4.9)$$

4.1.2 Update

The Kalman gain \mathbf{K} is computed based upon the current state covariance, the instantaneous linearization of the observation model \mathbf{h} , and expected covariance of observation noise \mathbf{R} :

$$\mathbf{K}_j = \mathbf{P}_{j|j-1} \mathbf{H}_j^\top (\mathbf{H}_j \mathbf{P}_{j|j-1} \mathbf{H}_j^\top + \mathbf{R})^{-1}, \quad (4.10)$$

where $\mathbf{P}_{j|j-1}$ is the a priori estimate of \mathbf{P} found in (4.7) and

$$\mathbf{H}_j = \left. \frac{\partial \mathbf{h}}{\partial \mathbf{x}} \right|_{\bar{\mathbf{x}}_{j|j-1}}. \quad (4.11)$$

Once the Kalman gain has been determined, a correction to the a priori state estimate can be made. The correction is calculated by comparing the sensor readings \mathbf{z} with the expected

sensor readings corresponding to the a priori state estimate using the observation function $\mathbf{h}(\bar{\mathbf{x}}_{j|j-1})$:

$$\bar{\mathbf{x}}_{j|j} = \bar{\mathbf{x}}_{j|j-1} + \mathbf{K}_j(\mathbf{z}_j - \mathbf{h}(\bar{\mathbf{x}}_{j|j-1})). \quad (4.12)$$

Similarly, the covariance of the state estimate can be corrected based upon the a priori covariance of the state estimate, linearization of the observation model, and computed Kalman gain:

$$\mathbf{P}_{j|j} = (\mathbf{I} - \mathbf{K}_j\mathbf{H}_j)\mathbf{P}_{j|j-1}. \quad (4.13)$$

4.2 Implementing the Hybrid Extended Kalman Filter

Equation (4.1) predicts how the state evolves through the function $\mathbf{f}(\mathbf{x}, \mathbf{u})$ using the system's current state \mathbf{x} and the external input \mathbf{u} . In order to perform accurate state estimation, an accurate model of the system's dynamics must be formed.

4.2.1 Dynamics

The net applied torque $\boldsymbol{\tau}_m$ on the actuator magnet is related to the magnet's instantaneous angular velocity $\boldsymbol{\omega}_m$ and angular acceleration $\dot{\boldsymbol{\omega}}_m$ by

$$\boldsymbol{\tau}_m = \mathbf{J}\dot{\boldsymbol{\omega}}_m + \mathbf{B}(\boldsymbol{\omega}_m)\boldsymbol{\omega}_m + \mathbf{c}(\boldsymbol{\omega}_m, \boldsymbol{\tau}_m), \quad (4.14)$$

where the manipulator's rotational inertia matrix is denoted by $\mathbf{J} \in \mathbb{R}^{3 \times 3}$, the viscous friction matrix is $\mathbf{B}(\boldsymbol{\omega}_m) \in \mathbb{R}^{3 \times 3}$, and the Coulomb friction is denoted by $\mathbf{c}(\boldsymbol{\omega}_m, \boldsymbol{\tau}_m) \in \mathbb{R}^3$. Solving for $\dot{\boldsymbol{\omega}}_m$ yields

$$\dot{\boldsymbol{\omega}}_m = \mathbf{J}^{-1}(\boldsymbol{\tau}_m - \mathbf{B}(\boldsymbol{\omega}_m)\boldsymbol{\omega}_m - \mathbf{c}(\boldsymbol{\omega}_m, \boldsymbol{\tau}_m)). \quad (4.15)$$

The combined rotational inertia matrix \mathbf{J} is given as

$$\mathbf{J} = \mathbf{J}_m + \eta^2 \mathbf{J}_w, \quad (4.16)$$

where gear ratio η and transmission matrix \mathbf{A} are defined in Sections (2.6) and (2.8), respectively. The magnet's rotational inertia matrix \mathbf{J}_m is defined as

$$\mathbf{J}_m = \frac{2}{5}m_m r_m^2 \mathbf{I}_3, \quad (4.17)$$

where m_m is the mass of the spherical magnet and r_m is its radius. The rotational inertia of each omniwheel is modeled to include the rotating omniwheel's inertia (approximated as a rotating disk with radius r_w and mass m_w) and the corresponding driving motor's inertia

j_{mot} (this term includes the motor's rotor inertia reflected through any gearing in the motor, as seen at the output shaft), which are packed into a diagonal matrix of the form

$$\mathbf{J}_w = \left(\frac{1}{2} m_w r_w^2 + j_{mot} \right) \mathbf{I}_3. \quad (4.18)$$

Experimentally, we have observed viscous and Coulomb friction effects [31] that are asymmetric in nature. The viscous friction matrix $\mathbf{B}(\omega_m)$ is modeled as $\mathbf{B} = \text{diag}(B_1, B_2, B_3)$ where the coefficients B_i are determined according to the sign of the corresponding terms of ω_m :

$$B_i = \begin{cases} B_i^+ : \omega_{m,i} > 0 \\ B_i^- : \omega_{m,i} < 0 \end{cases} \quad (4.19)$$

The Coulomb friction term $\mathbf{c}(\omega_m, \tau_m)$, which models static friction, is defined as

$$c_i = \begin{cases} \tau_i : \omega_{m,i} = 0 \text{ and } c_i^- \leq \tau_{m,i} \leq c_i^+ \\ c_i^+ : \omega_{m,i} = 0 \text{ and } \tau_{m,i} > c_i^+ \\ c_i^- : \omega_{m,i} = 0 \text{ and } \tau_{m,i} < c_i^- \\ c_i^+ : \omega_{m,i} > 0 \\ c_i^- : \omega_{m,i} < 0 \end{cases} \quad (4.20)$$

Equations (4.19) and (4.20) are illustrated in Figs. 4.1(a) and 4.1(b), respectively. The coefficients B_i and c_i are determined experimentally and discussed in Chapter 6.

4.2.2 Sources of Imprecision

Imprecision manifests itself as either measurement noise or process noise. Measurement noise is a phenomenon that is directly measured by sensors and its covariance is reflected in the covariance matrix $\mathbf{R} \in \mathbb{R}^{p \times p}$, where p is the dimension of the sensor space ($\mathbf{z} \in \mathbb{R}^p$). Process noise is the other primary classification of imperfection, whose covariance is estimated in $\mathbf{Q} \in \mathbb{R}^{n \times n}$, where n is the dimension of the state space ($\mathbf{x} \in \mathbb{R}^n$).

4.2.2.1 Measurement Noise

Each of the sensors employed in the SAMM contribute to the overall noise. The sensor space encapsulates the cluster of six Hall-effect sensors, as well a measurement of ω_a obtained from the motors' encoders using (2.6). Noise measured by the Hall-effect sensors could be the result of perturbations in the magnetic field (e.g., due to magnetization of soft-magnetic material near the sensor) or due to analog-to-digital conversion. The measurement of ω_m is retrieved by querying the Maxon-Motor drivers, causing it to suffer differentiation errors (i.e., converting encoder position counts to angular-velocity),

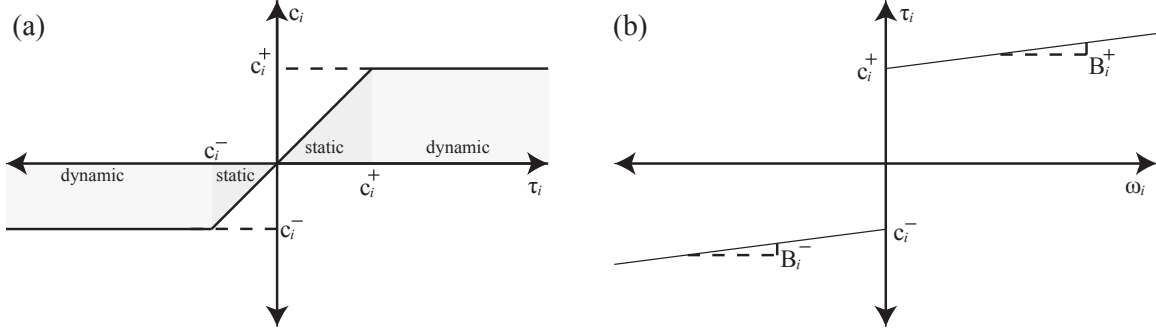


Figure 4.1. Illustration of the observed asymmetric viscous and Coulomb friction. Behavior of c_i that models asymmetric Coulomb friction is depicted in (a). Asymmetric viscous friction, modeled by B_i , is shown in (b).

analog signal noise (since the velocity signal is transmitted as an analog voltage from the Maxon-Motor controllers to the Sensoray DAC card), and quantization errors (from converting the analog voltage to a digital signal). Noise from each sensor is assumed to be both zero-mean and Gaussian.

4.2.2.2 Process Noise

Physical disturbances, unintended magnetic torque, and modeling errors are all sources of process noise. Physical disturbances may manifest from unintentional mechanical binding or slipping. Any magnetized material near the spherical magnet could generate an unintended magnetic torque. Modeling errors arise any time one of the assumptions outlined in Chapter 2 are violated (e.g., the assumption of no-slip between the omniwheels and magnet). Additionally, modeling errors accrue due to imperfections in modeling of the physical components (e.g., inaccuracies of the modeled magnet mass m_m as compared to its actual mass, misalignments in the omniwheel axes $\hat{\mathbf{a}}_i$). Process-noise effects are more nuanced and difficult to directly measure than noise in the sensor space. Due to this, a conservative estimate on each of the parameters is employed here. Further work should utilize techniques such as *System Identification* and *Expectation-Maximization* in order to more accurately characterize these effects.

4.2.3 Hybrid EKF Implementation for the SAMM

The SAMM's state is represented as

$$\mathbf{x} = \begin{bmatrix} \hat{\mathbf{m}} \\ \boldsymbol{\omega}_m \end{bmatrix} \in \mathbb{S}^2 \times \mathbb{R}^3. \quad (4.21)$$

Where $\hat{\mathbf{m}} \in \mathbb{S}^2$ is the unit-length dipole heading, and $\boldsymbol{\omega}_m \in \mathbb{R}^3$ is the angular velocity of the actuator magnet. The state-transition model is linearized to form the Jacobian \mathbf{F} . Taking

the time derivative of the state (4.21) yields the state transition equation:

$$\dot{\mathbf{x}} = \begin{bmatrix} \dot{\hat{\mathbf{m}}} \\ \dot{\boldsymbol{\omega}}_{\mathbf{m}} \end{bmatrix} = \mathbf{f} \left(\begin{bmatrix} \hat{\mathbf{m}} \\ \boldsymbol{\omega}_{\mathbf{m}} \end{bmatrix}, \boldsymbol{\tau}_{\mathbf{m}} \right) = \mathbf{f}(\mathbf{x}, \mathbf{u}). \quad (4.22)$$

Geometrically $\dot{\hat{\mathbf{m}}}$ can be found as

$$\dot{\hat{\mathbf{m}}} = \boldsymbol{\omega}_{\mathbf{m}} \times \hat{\mathbf{m}}. \quad (4.23)$$

The nonlinear state transition function \mathbf{f} can be found from (4.23) and (4.15) yielding:

$$\dot{\mathbf{x}} = \begin{bmatrix} \boldsymbol{\omega}_{\mathbf{m}} \times \hat{\mathbf{m}} \\ \mathbf{J}^{-1}(\boldsymbol{\tau}_{\mathbf{m}} - \mathbf{B}(\boldsymbol{\omega}_{\mathbf{m}})\boldsymbol{\omega}_{\mathbf{m}} - \mathbf{c}(\boldsymbol{\omega}_{\mathbf{m}}, \boldsymbol{\tau}_{\mathbf{m}})) \end{bmatrix}, \quad (4.24)$$

where \mathbf{J} in the prototype instantiation of the SAMM is calculated using (4.16) to be

$$\mathbf{J} = \begin{bmatrix} 1.39 & 0.00 & 0.00 \\ 0.00 & 1.39 & 0.00 \\ 0.00 & 0.00 & 1.39 \end{bmatrix} 10^{-4} \text{ kg} \cdot \text{m}^2$$

as a result of the spherical magnet's mass and radius ($m_m = 0.515 \text{ kg}$ and $r_m = 0.0254 \text{ m}$, respectively), the omniwheels' mass and radius ($m_w = 0.0262 \text{ kg}$ and $r_w = 0.0286 \text{ m}$, respectively), and the inertia of the motors reflected through their gearhead ($j_{mot} = 0.0755 \text{ kg} \cdot \text{m}^2$). The applied torque on the magnet $\boldsymbol{\tau}_{\mathbf{m}}$ (the input \mathbf{u} to the SAMM system) is estimated using current feedback obtained from the Maxon Motor drivers in conjunction with the motor torque constant (47.5 mNm/A), which is mapped from motor space to magnet space using (2.8).

The linearization \mathbf{F} is given by

$$\mathbf{F} = \left. \frac{\partial \mathbf{f}}{\partial \mathbf{x}} \right|_{\bar{\mathbf{x}}, \mathbf{u}} = \begin{bmatrix} \{\boldsymbol{\omega}_{\mathbf{m}}\} & -\{\hat{\mathbf{m}}\} \\ \mathbf{0} & -\mathbf{J}^{-1}\mathbf{B}(\boldsymbol{\omega}_{\mathbf{m}}) \end{bmatrix}. \quad (4.25)$$

Recall that notation involving curly braces denotes a skew-symmetric matrix as defined in (2.4). Note that the Coulumb friction term $\mathbf{c}(\boldsymbol{\omega}_{\mathbf{m}}, \boldsymbol{\tau}_{\mathbf{m}})$ does not vary with $\hat{\mathbf{m}}$ or $\boldsymbol{\omega}_{\mathbf{m}}$ when $\boldsymbol{\omega}_{\mathbf{m}} \neq \mathbf{0}$. Both $\mathbf{B}(\boldsymbol{\omega}_{\mathbf{m}})$ and $\mathbf{c}(\boldsymbol{\omega}_{\mathbf{m}}, \boldsymbol{\tau}_{\mathbf{m}})$ are not differentiable when $\boldsymbol{\omega}_{\mathbf{m}} = \mathbf{0}$ but we neglect this issue since $\boldsymbol{\omega}_{\mathbf{m}}$ is rarely $\mathbf{0}$.

The observation model is structured as

$$\mathbf{z} = \mathbf{h}(\mathbf{x}) = \begin{bmatrix} \mathbf{S} \|\mathbf{m}\| & \mathbf{0} \\ \mathbf{0} & \mathbf{I}_3 \end{bmatrix} \mathbf{x}, \quad (4.26)$$

utilizing \mathbf{S} defined in (2.11). The observation model $\mathbf{h}(\mathbf{x})$ is then linearized as

$$\mathbf{H} = \frac{\partial \mathbf{h}}{\partial \mathbf{x}} = \begin{bmatrix} \mathbf{S} \|\mathbf{m}\| & \mathbf{0} \\ \mathbf{0} & \mathbf{I}_3 \end{bmatrix}. \quad (4.27)$$

4.2.4 Numerical Integration

The integrals in (4.6) and (4.7), which compute the a priori estimates $\mathbf{x}_{j|j-1}$ and $\mathbf{P}_{j|j-1}$, respectively, are performed using a fourth-order Runge-Kutta method [30]. For example, to compute (4.6), where $\dot{\mathbf{x}} = \mathbf{f}(\mathbf{x}, \mathbf{u})$ and using a step size of $\delta = t_j - t_{j-1}$, $\mathbf{x}_{j|j-1}$ can be estimated as

$$\mathbf{x}_{j|j-1} = \mathbf{x}_{j-1|j-1} + \frac{\delta}{6}(\mathbf{k}_1 + 2\mathbf{k}_2 + 2\mathbf{k}_3 + \mathbf{k}_4), \quad (4.28)$$

where the values are found as

$$\mathbf{k}_1 = \mathbf{f}(\mathbf{x}_{j-1|j-1}, \boldsymbol{\tau}_{\mathbf{m},j-1}), \quad (4.29)$$

$$\mathbf{k}_2 = \mathbf{f}\left(\left(\mathbf{x}_{j-1|j-1} + \frac{\delta}{2}\mathbf{k}_1\right), \boldsymbol{\tau}_{\mathbf{m},j-1}\right), \quad (4.30)$$

$$\mathbf{k}_3 = \mathbf{f}\left(\left(\mathbf{x}_{j-1|j-1} + \frac{\delta}{2}\mathbf{k}_2\right), \boldsymbol{\tau}_{\mathbf{m},j-1}\right), \quad (4.31)$$

$$\mathbf{k}_4 = \mathbf{f}\left(\left(\mathbf{x}_{j-1|j-1} + \delta\mathbf{k}_3\right), \boldsymbol{\tau}_{\mathbf{m},j-1}\right). \quad (4.32)$$

Note that the Runge-Kutta step size δ corresponds to one Kalman iteration in our implementation. If greater accuracy is required, δ can be made much smaller so that more Runge-Kutta steps are used.

CHAPTER 5

CONTROL

The SAMM has two modes of operation: *pointing* and *rotating*. Examples of where the pointing mode would be useful include any tasks requiring quasistatic magnetic fields such as the actuation of an endoscopic capsule in the stomach [15,16], a magnet-tipped catheter [17], or a magnet-tipped cochlear-implant electrode array [18]. Examples of where the rotating mode would be useful include any task where a rotating magnetic field is fundamental to the actuation strategy, such as rolling UMDs along a surface [5–7], swimming through a fluid or crawling through a lumen via helical propulsion [8–12], or screwing through soft tissue [13].

A high-level system diagram illustrating the flow of information through the SAMM’s subsystems is shown in Fig. 5.1. The Maxon-Motor controllers takes as input a desired motor angular velocity, but since they act on that input in a model-based open-loop fashion (in our chosen implementation), there is no guarantee that the motor’s angular velocity will achieve the desired, necessitating the inclusion of our own custom controller. The pointing-mode and rotating-mode controllers output a necessary magnet angular velocity

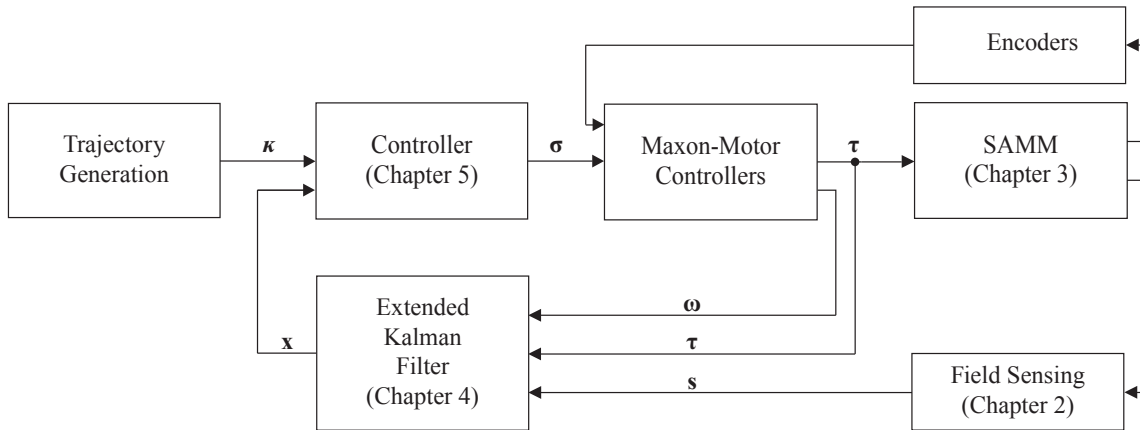


Figure 5.1. System diagram used for control of the SAMM.

σ , which is mapped to the motor-space by the transmission matrix \mathbf{A} .

5.1 Pointing-Mode Controller

The pointing-mode controller governs the *heading* of the actuator-magnet dipole moment $\hat{\mathbf{m}}$ to align along a desired heading $\hat{\kappa} \in \mathbb{S}^2$. A proportional-integral-derivative (PID) heading-control scheme is employed (see Fig. 5.2) using the Kalman filter's estimate of the dipole moment $\hat{\mathbf{m}}$. In order to drive $\hat{\mathbf{m}}$ toward $\hat{\kappa}$, the heading's restoration vector \mathbf{e} is computed as

$$\mathbf{e} = \hat{\mathbf{m}} \times \hat{\kappa}, \quad (5.1)$$

where “ \mathbf{e} ” was chosen to connote “error,” which it does approximate at small angles, although it does not define the error in general. At small misalignments \mathbf{e} is approximately linearly proportional to angular misalignment, although it becomes increasingly nonlinear at large misalignments. Control effort $\sigma_j \in \mathbb{R}^3$ at time-sample j is computed as

$$\sigma_j = k_p \mathbf{e}_j + k_i (\mathbf{I}_3 - \hat{\mathbf{m}} \hat{\mathbf{m}}^\top) \mathbf{q}_\epsilon(\mathbf{e}_j) + k_d \text{sat}_v \left(\frac{\mathbf{e}_j - \mathbf{e}_{j-1}}{\delta} \right), \quad (5.2)$$

where k_p , k_i , and k_d are the proportional, integral, and derivative PID-controller gains, respectively. The integral term $\mathbf{q}_\epsilon(\mathbf{e}_j)$, which is capped at ϵ to prevent integrator wind-up, is computed as

$$\mathbf{q}_\epsilon(\mathbf{e}_j) = \begin{cases} \mathbf{q}_\epsilon(\mathbf{e}_{j-1}) + \delta \mathbf{e}_j : & \|\mathbf{q}_\epsilon(\mathbf{e}_{j-1}) + \delta \mathbf{e}_j\| \leq \epsilon \\ \mathbf{q}_\epsilon(\mathbf{e}_{j-1}) : & \|\mathbf{q}_\epsilon(\mathbf{e}_{j-1}) + \delta \mathbf{e}_j\| > \epsilon \end{cases}, \quad (5.3)$$

where δ is the time step as defined previously. The term $(\mathbf{I}_3 - \hat{\mathbf{m}} \hat{\mathbf{m}}^\top)$ in (5.2) has the function of removing any component of the integrated error that is parallel to $\hat{\mathbf{m}}$, such that only productive motion commands are sent to the motors (since rotating the spherical magnet about $\hat{\mathbf{m}}$ has no effect on the resulting field). The saturation function acts on the norm of the input vector to preserve its direction, and is defined as:

$$\text{sat}_v(\mathbf{z}) = \begin{cases} \mathbf{z} : & \|\mathbf{z}\| \leq v \\ \hat{\mathbf{z}} v : & \|\mathbf{z}\| > v \end{cases}. \quad (5.4)$$

The saturation function used on the derivative term removes noise spikes that lead to undesirable behavior.

5.2 Rotating-Mode Controller

The purpose of the rotating-mode controller is to generate continuous rotation of the actuator-magnet dipole with some desired angular velocity κ , with the dipole orthogonal to κ , without any concern for the phase of the dipole within the cycle. The rotating

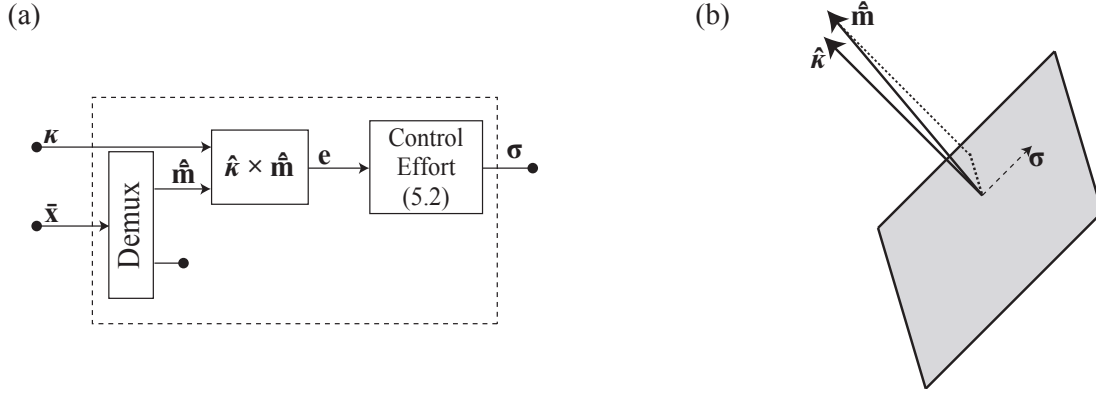


Figure 5.2. A graphical depiction of the PID heading-control described herein. Control law shown in (a) represents the Controller block in Fig. 5.1 when performing pointing-mode control. The controller attempts to align the dipole estimate $\hat{\mathbf{m}}$ to the desired input direction $\hat{\kappa}$. The resulting control effort σ is depicted in (b), attempting to align the dipole $\hat{\mathbf{m}}$ with the input $\hat{\kappa}$.

mode simultaneously employs two control laws: a PI-plus-feed-forward angular velocity subcontroller that rotates $\hat{\mathbf{m}}$ about a desired angular velocity vector κ with control effort given by σ_{\parallel} , which is *parallel* to κ , and a PD heading subcontroller to drive $\hat{\mathbf{m}}$ to the plane *orthogonal* to κ with control effort given by σ_{\perp} . These controllers are independent from each other, as they always actuate orthogonal to one another. The two orthogonal control laws are combined to form the total output

$$\sigma = \sigma_{\parallel} + \sigma_{\perp}. \quad (5.5)$$

To determine control effort in the direction parallel to κ , the angular-velocity error \mathbf{e}_{\parallel} , denoted in Fig. 5.3(a) simply as Velocity Error, must first be computed. Angular-velocity error is given by

$$\mathbf{e}_{\parallel} = \kappa - (\bar{\omega}_{\mathbf{m}} \cdot \hat{\kappa}) \hat{\kappa}. \quad (5.6)$$

Control effort in the direction parallel to κ , which governs angular velocity, can then be computed at time-sample j as

$$\sigma_{\parallel,j} = \kappa_j + k_{p\parallel} \mathbf{e}_{\parallel,j} + k_{i\parallel} (\mathbf{q}_{\epsilon}(\mathbf{e}_{\parallel,j}) \cdot \hat{\kappa}_j) \hat{\kappa}_j, \quad (5.7)$$

where the “ κ ” term represents a feed-forward component, and the behavior of the capped integration function \mathbf{q}_{ϵ} is defined in (5.3). The term \mathbf{q}_{ϵ} is projected onto the rotation axis parallel to κ to alleviate the effects of integrator wind-up in what is currently the wrong direction.

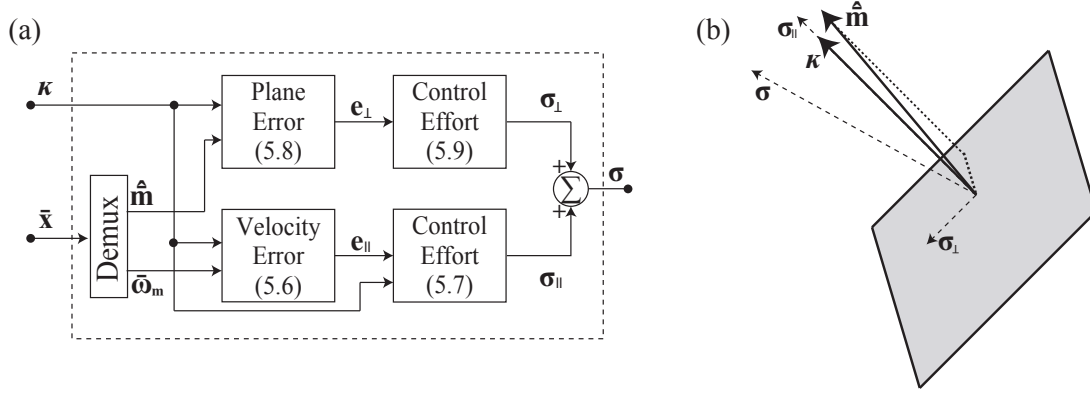


Figure 5.3. A graphical depiction of the rotation controller operation described herein. The control law shown in (a) represents the Controller block in Fig. 5.1 when performing rotating-mode control. The rotating mode attempts to drive the angular velocity of the dipole moment estimate $\hat{\mathbf{m}}$ to some desired angular velocity input $\boldsymbol{\kappa}$ while driving the estimate of the dipole moment $\hat{\mathbf{m}}$ to be orthogonal to given input $\boldsymbol{\kappa}$. The resulting control efforts depicted in (b) illustrate how the two orthogonal subcontrollers combine to form the total control effort $\boldsymbol{\sigma}$. The component driving the dipole toward the plane orthogonal to the input is illustrated by $\boldsymbol{\sigma}_\perp$, and the component rotating the dipole about the input is illustrated by $\boldsymbol{\sigma}_\parallel$.

Rotation-plane restoration vector \mathbf{e}_\perp , denoted in Fig. 5.3(a) simply as Plane Error, and with an analogous relationship to error as described with (5.1), is found as

$$\mathbf{e}_\perp = \hat{\mathbf{m}} \times (\mathbf{I}_3 - \hat{\boldsymbol{\kappa}}\hat{\boldsymbol{\kappa}}^\top)\hat{\mathbf{m}}. \quad (5.8)$$

Control effort in the direction perpendicular to $\boldsymbol{\kappa}$ can then be computed at time-sample j as

$$\boldsymbol{\sigma}_{\perp,j} = \xi_j \left(k_{p\perp} \|\mathbf{e}_{\perp,j}\| \xi_j + k_{d\perp} \text{sat}_v \left(\frac{\|\mathbf{e}_{\perp,j}\| \xi_j - \|\mathbf{e}_{\perp,j-1}\| \xi_{j-1}}{\delta} \right) \right) \hat{\mathbf{e}}_{\perp,j}, \quad (5.9)$$

where

$$\xi_j = \text{sgn}(\bar{\boldsymbol{\omega}}_{\mathbf{m},j} \cdot \hat{\mathbf{m}}_j) \quad (5.10)$$

is a signum function that is used to correctly account for signed rotation-plane error (i.e., determine if $\hat{\mathbf{m}}$ is above or below the desired plane), the gains $k_{p\perp}$ and $k_{d\perp}$ are proportional and derivative gains, and time step δ is the same as previously defined. The inclusion of the signum function is necessary because the direction of \mathbf{e}_\perp , computed with (5.8), flips when the dipole crosses through the desired plane. The saturation function sat_v acts as defined in (5.4). The gains $k_{p\perp}$ and $k_{d\perp}$ first act upon the *magnitude* of the rotation-plane restoration vector $\|\mathbf{e}_\perp\|$ and are then applied in the *direction* of the rotation-plane restoration vector $\hat{\mathbf{e}}_\perp$.

CHAPTER 6

EXPERIMENTATION

All of the following experiments were performed with the SAMM mounted to a 6-DOF Yaskawa Motoman robotic arm, which is housed in an enclosure to aid in minimizing environmental disturbances. The robotic arm was stationary during all testing and oriented in a “vertical” orientation as shown in Fig. 6.1.

The control system and data recording for these experiments was implemented in C++, with a Sensoray Model 626 PCI DAQ card as the hardware interface to the SAMM. The



Figure 6.1. Experimental setup showing orientation and mounting of SAMM onto a 6-DOF Yaskawa Motoman robotic arm.

SAMM's control system is designed in a multithreaded structure with the control loop, the Kalman-estimator loop, and the SAMM I/O loop all operating at 1000 Hz.

6.1 Parameter Estimation

Many of the parameters in this SAMM implementation are theoretically calculated, such as the transmission matrix \mathbf{A} , where there is a clear means of approximating its elements. Other parameters such as the directional Coulomb and viscous friction terms (\mathbf{c} and \mathbf{B} , respectively) were empirically determined.

6.1.1 Coulomb and Viscous Friction

Friction in the SAMM was estimated using a directional Coulomb-plus-viscous friction model described in Section 4.2.1. The friction parameters were experimentally obtained by driving the motors at open-loop velocities ranging, in discrete increments, from 0 to 2π rad/s. Each increment lasted for 30 seconds while the resulting motor torque (τ_a) and sensed motor angular velocity (ω_a) were recorded at a rate of 20 Hz. The motor torque and sensed angular velocity data were averaged and plotted as shown in Fig. 6.2. A line was fit to the data, using least-squares, whose y-intercept and slope corresponding to the Coulomb friction (\mathbf{c}) and viscous friction (\mathbf{B}), respectively. The least-squares-fit lines are plotted in Fig. 6.2, and the values for \mathbf{c} and \mathbf{B} were numerically found to be

$$\mathbf{B}^+ = \begin{bmatrix} 0.0001 & 0.0 & 0.0 \\ 0.0 & 0.0014 & 0.0 \\ 0.0 & 0.0 & 0.0001 \end{bmatrix} \text{ N} \cdot \text{s/rad},$$

$$\mathbf{B}^- = \begin{bmatrix} 0.00001 & 0.0 & 0.0 \\ 0.0 & 0.0014 & 0.0 \\ 0.0 & 0.0 & 0.0005 \end{bmatrix} \text{ N} \cdot \text{s/rad},$$

$$\mathbf{c}^+ = \begin{bmatrix} 0.0632 \\ 0.0411 \\ 0.0436 \end{bmatrix} \text{ N}, \mathbf{c}^- = \begin{bmatrix} -0.0455 \\ -0.0330 \\ -0.0723 \end{bmatrix} \text{ N}.$$

6.1.2 Sensor Noise

Noise from each of the sensors is modeled with the observation covariance matrix \mathbf{R} described in Section 4.2.2. The submatrix of \mathbf{R} that corresponds to the Hall-sensor covariance is directly estimated by removing the spherical magnet from the SAMM and reading the idle sensor values to determine their intrinsic noise. The submatrix corresponding to

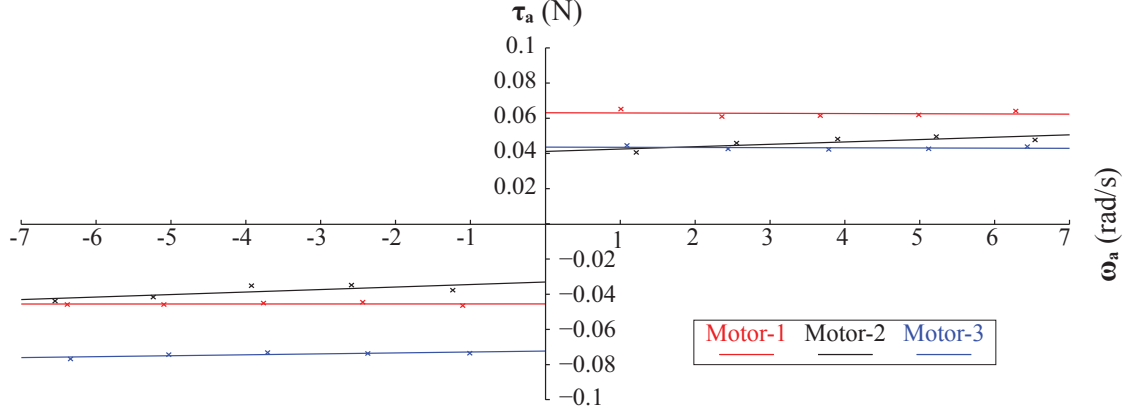


Figure 6.2. Experimental data showing motor torque ($\tau_{a,i}$) versus motor angular velocity ($\omega_{a,i}$), with Coulomb-plus-viscous friction fit.

the angular-velocity-measurement covariance is measured by recording the covariance of the angular-velocity sensor values with the motors driven open-loop with a constant input (which we assume results in approximately constant motor angular velocity). In both cases, sensor data are collected at a rate of 20 Hz for a duration of ~ 10 minutes. The covariances and means of the first 50% of the data were compared to the final 50% to ensure that the estimation had converged and enough data were collected. Each sensor was independently evaluated for a DC offset, which is then removed in implementation to ensure that the noise measured by each sensor is zero-mean. Note that we assume the Hall-sensor measurements to be independent from the angular-velocity measurements, which causes the off-diagonal terms of \mathbf{R} to be zero. The observation covariance measured and implemented in the prototype instantiation of the SAMM is

$$\mathbf{R} = \begin{bmatrix} 2.9 & 0.0 & 0.0 & 0.0 & 0.0 & 0.0 & 0.0 & 0.0 & 0.0 \\ 0.0 & 2.9 & 0.0 & 0.0 & 0.0 & 0.0 & 0.0 & 0.0 & 0.0 \\ 0.0 & 0.0 & 2.9 & 0.0 & 0.0 & 0.0 & 0.0 & 0.0 & 0.0 \\ 0.0 & 0.0 & 0.0 & 2.8 & 0.0 & 0.0 & 0.0 & 0.0 & 0.0 \\ 0.0 & 0.0 & 0.0 & 0.0 & 2.9 & 0.0 & 0.0 & 0.0 & 0.0 \\ 0.0 & 0.0 & 0.0 & 0.0 & 0.0 & 2.8 & 0.0 & 0.0 & 0.0 \\ 0.0 & 0.0 & 0.0 & 0.0 & 0.0 & 0.0 & 6.0 & 0.0 & 0.0 \\ 0.0 & 0.0 & 0.0 & 0.0 & 0.0 & 0.0 & 0.0 & 6.0 & 0.0 \\ 0.0 & 0.0 & 0.0 & 0.0 & 0.0 & 0.0 & 0.0 & 0.0 & 6.0 \end{bmatrix} \cdot 10^{-3},$$

where the units of the top-left 6×6 submatrix of \mathbf{R} is mT^2 , and the bottom-right 3×3 submatrix of \mathbf{R} have units rad^2/s^2 . The off-diagonal terms in the bottom-right 3×3 submatrix are measured to be near zero, making the angular-velocity measurements independent.

6.1.3 Process Noise

Process noise, represented by the covariance matrix \mathbf{Q} , is difficult to measure without the aid of techniques such as *System Identification* or the *Expectation-Maximization* algorithm. Because of this, we experimentally tuned the process-noise covariance to produce desirable tracking performance. The process-update covariance qualitatively conceived and implemented in the prototype instantiation of the SAMM is

$$\mathbf{Q} = \begin{bmatrix} 0.002 & 0.0 & 0.0 & 0.0 & 0.0 & 0.0 \\ 0.0 & 0.002 & 0.0 & 0.0 & 0.0 & 0.0 \\ 0.0 & 0.0 & 0.002 & 0.0 & 0.0 & 0.0 \\ 0.0 & 0.0 & 0.0 & 2.0 & 0.0 & 0.0 \\ 0.0 & 0.0 & 0.0 & 0.0 & 2.0 & 0.0 \\ 0.0 & 0.0 & 0.0 & 0.0 & 0.0 & 2.0 \end{bmatrix}.$$

The top-left 3×3 submatrix, which corresponds to heading uncertainty, was held to δ (0.001 in the prototype SAMM) times the value used in the bottom-right 3×3 submatrix, which in turn corresponds to the magnet’s angular-velocities uncertainty; the rationale behind this choice is that dipole heading is estimated by integrating angular-velocity over one time step, so angular-velocity error is mapped to heading error in a predictable way. This constraint reduced the tuning search to a 1-DOF search. Similar to the structure of \mathbf{R} , the off-diagonal terms of \mathbf{Q} have been set to zero as we assume all of the states to be independent. The units of \mathbf{Q} correspond to the units of the state, where the upper-left block matrix denotes the covariance of the dipole heading (which is a unitless heading on the unit-sphere), and the lower-right block matrix is the covariance of the dipole’s angular velocity measured in rad^2/s^2 .

6.2 Controller Tuning

6.2.1 Ziegler-Nichols Tuning of the Heading Controllers

In order to implement the PID pointing-mode controller and the PD “orthogonal” rotating-mode controller, which are both effectively forms of heading regulation, we must select the respective controller gains. The Ziegler-Nichols tuning method is a heuristic-based approach to tuning PID controllers. The method involves creating a P-controller and slowly increasing its gain until marginal stability is observed (i.e., when the experimentally observed oscillations are neither decreasing nor increasing over time). This gain defines the “ultimate gain” k_u , and the period of the resulting oscillations defines the “ultimate period” t_u . These identified parameters, which are specific to the SAMM for a given magnitude of step input (since the SAMM is not a linear system), are used to determine all of the relevant

k_p , k_i , and k_d gains. The tuning parameters k_u and t_u were experimentally found to be 21.5 rad/s and 0.65 s, respectively, when tuning for a step-input magnitude of 5° .

Different PID implementations were evaluated for their time-response to step inputs and error-rejection capabilities. The *Pessen integral* PID formulation [32] was compared with *classic*, *some-overshoot*, and *no-overshoot* PID formulations. Pessen noted in [32] that the Ziegler-Nichols tuning method was not developed for noninteracting controllers (i.e., it was developed for ideal PID controllers), and he therefore proposed his alternate formula, which is also based on k_u and t_u . The Pessen-integral PID formulation had the most desirable transient response; the other formulations were either deemed qualitatively too oscillatory or were slower to converge on the steady-state value.

The resulting PID gains based on the Pessen-integral formulation are given in Table 6.1. Appropriate PD controller gains for the orthogonal components of the rotating-mode controller can be obtained using the same ultimate gain and ultimate period as used above. The results are also shown in Table 6.1. The PD controller uses a higher proportional gain than the PID controller in exchange for the lack of an integral term and a slightly higher derivative gain. It was found that for both the Pessen-integral PID and PD controllers with steps of 25° or less, the settling time t_s was approximately 1.5 s, which is equivalent to a time constant of approximately $\tau = 0.3$ s. The time-constant began to slow at steps larger than 25° . This may be attributed partially to the nonlinear nature of heading control on the unit-sphere, and partially due to nonidealities in the physical device (e.g., larger steps incite a larger control effort, which could lead to slipping of the omniwheels relative to the magnetic sphere). A plot illustrating the time response to the given step inputs for the PD controller is shown in Fig. 6.3 and for the PID is shown in Fig. 6.4. Note that, due to nonlinearities in the system, the integrator in the PID controller never fully rejects the steady-state error of approximately 21.0 mrad (1.2°).

Table 6.1. Gains calculated for Pessen-integral PID and PD controllers based on the measured k_u and t_u parameters found during the Ziegler-Nichols tuning method.

	$k_p(\text{rad/s})$		$k_i(\text{rad/s}^2)$		$k_d(\text{rad})$	
	formula	value	formula	value	formula	value
Pessen-integral PID	$0.7k_u$	15.1	$0.4k_p/t_u$	9.27	$0.15k_p t_u$	1.41
PD	$0.8k_u$	17.2	—	—	$k_p t_u/8$	1.40

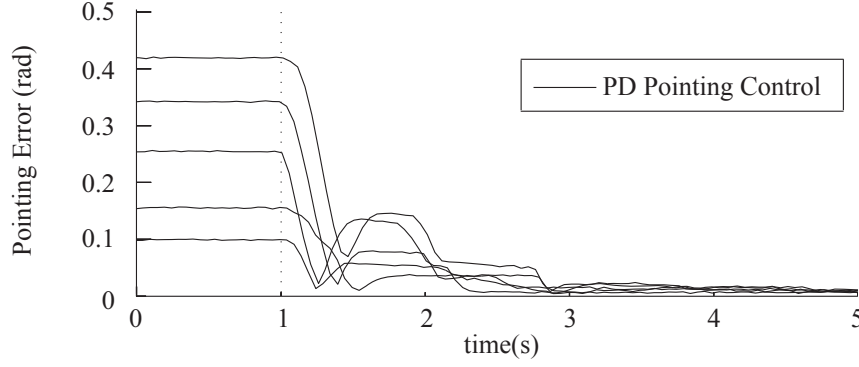


Figure 6.3. PD controller settling time for step inputs spanning 0.087 to 0.463rad (5 to 25 deg). The controller remains off for the first 1 s of the test, at which time it begins to regulate the error. Using a 5% settling criteria, the time constant τ was found to be approximately 0.3 s.

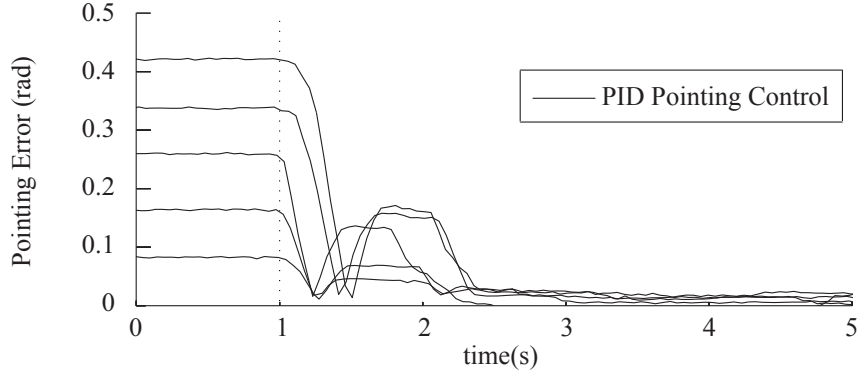


Figure 6.4. PID controller settling time for step inputs spanning 0.087 to 0.463rad (5 to 25 deg). The controller remains off for the first 1 s of the test, at which time it begins to regulate the error. Using a 5% settling criteria, the time constant τ was found to be approximately 0.3 s. Note that, due to nonlinearities in the system, the integrator in the PID controller never fully rejects the steady-state error of approximately 21.0 mrad (1.2°).

6.2.2 Tuning of the Angular-Velocity Controller

When tuning the PI-plus-feed-forward subcontroller of the rotation-mode controller, Ziegler-Nichols tuning is no longer relevant because of the system's first-order behavior. Therefore a different tuning technique was used. It was determined that it would be desirable for the angular-velocity subcontroller and heading subcontroller (i.e., the orthogonal component that regulates the rotating dipole to be orthogonal to the angular-velocity vector) to converge about their respective set-points with similar time constants. To accomplish this, the angular-velocity subcontroller's closed-loop poles were tuned accordingly.

The velocity-controlled sphere can be modeled as a simple first-order mass-damper system. The time constant τ , friction b_{eff} , and effective mass m_{eff} values may be determined from Table 6.2, with a resulting plant transfer function,

$$G(s) = \frac{1}{m_{eff}s + b_{eff}} = \frac{\frac{1}{b_{eff}}}{\frac{m_{eff}}{b_{eff}}s + 1}, \quad (6.1)$$

where $\tau = 0.464$ s, $b_{eff} = 0.0893$ N·s/rad, and $m_{eff} = 0.0414$ kg. For the proposed PI controller with transfer function,

$$C(s) = \frac{k_{p||}s + k_{i||}}{s}, \quad (6.2)$$

the resulting closed-loop characteristic equation can be approximated as

$$m_{eff}s^2 + (b_{eff} + k_{p||})s + k_{i||} = 0. \quad (6.3)$$

The characteristic equation describes the SAMM's dynamic response, and its poles may be set arbitrarily through the selection of $k_{p||}$ and $k_{i||}$. To achieve a system that is near critically damped, the two closed-loop poles should be set to be equal, providing the first constraint equation. Additionally, to yield a system where the angular-velocity subcontroller settles in approximately the same time as the heading subcontroller, the poles of the rotational-velocity subcontroller are selected to have the same time constant as that of the heading subcontroller, providing the second constraint equation. This yields the gains of $k_{p||} = 0.187$, and $k_{i||} = 0.460$ s⁻¹.

In each of the controller implementations described in Chapter 5, the derivative terms are saturated with the sat_ν function and the integral terms are capped with q_ϵ . The limits set for these functions were experimentally set, with the intent to minimally influence the regular operation of the controllers. The derivative terms were saturated at $\nu=100$, which allows the derivative to function unimpeded during the majority of its operation, only clipping the most extreme derivative spikes. The integral terms were capped at $\epsilon=1$. This allows the integral term to generally operate unimpaired and was rarely observed to grow large, but prevents excessive wind-up in extreme cases.

6.3 Performance Demonstrations

The experiments described in this section demonstrate the SAMM's capabilities. The pointing-mode and rotating-mode controllers are demonstrated separately.

6.3.1 Pointing Mode

In this section, we present a demonstration of the pointing-mode controller of Section 5.1 by first performing a regulatory operation where the SAMM minimizes its heading error

Table 6.2. Open-loop velocity commands, with resulting steady-state angular-velocity $\|\omega_{\mathbf{m}}\|_{ss}$ and settling time t_s , in directions corresponding to each omniwheel axis. Average settling time and steady-state angular-velocity across all directions and axes are 2.32s and 11.2rad/s, respectively.

step rad/s	motor -	t_s s	$\ \omega_{\mathbf{m}}\ _{ss}$ rad/s
10.0	+M1	2.33	11.00
10.0	-M1	2.32	11.12
10.0	+M2	2.32	11.35
10.0	-M2	2.32	11.34
10.0	+M3	2.32	11.24
10.0	-M3	2.32	11.11

about a quasi-static point, which may move, but generally not fast enough to excite the system’s dynamics, and next, a trajectory tracking operation where the dipole tracks a rapidly moving precomputed heading. Both experiments follow trajectories where the heading of the spherical magnet’s dipole moment is updated at a constant time step of $\delta = 40$ ms. In both experiments, the Ziegler-Nichols tuned PD controller is compared with the Ziegler-Nichols tuned PID using Pessen’s integration rule. The comparison is used to confirm the benefit of the inclusion of the integral term. Finally, we generate an experimental Bode plot of the system with the PID controller to describe the frequency response of the system.

Quasi-static regulation involves tracking a heading that may be static (i.e., step inputs) or may slowly move in time. The trajectory does not make abrupt movements or otherwise excite the system dynamics. In this task the dipole heading starting pose was the $[0, 0, 1]^T$ direction, and it was slowly rotated at a constant angular-velocity (0.2 rad/s) about an axis in the x-y plane until the dipole heading intersected the x-y plane of the coordinate system, as illustrated in Fig. 6.5. This was repeated for eight rotation axes in the x-y plane radially separated by $\pi/4$ radians with both the PD and the Pessen-integral PID controllers. The resulting trajectories are illustrated in Fig. 6.5. A table of each trial’s RMS error is provided in Table 6.3. The results clearly indicate superior performance from the Pessen-integral PID controller, which has significantly lower RMS error over the eight trials. This is likely due to the quasi-static nature of the test where the integrator has time to act on residual errors.

Next, a path was devised to demonstrate the SAMM’s ability to track a more torturous dynamic trajectory. This trajectory was a “figure-8” (or lemniscate) projected onto the unit-sphere and positioned such that its intersection point is at $[0, 0, 1]^T$ and its extremes are in the $\pm y$ direction. Once the trajectory was projected onto the unit-sphere, it was parameterized

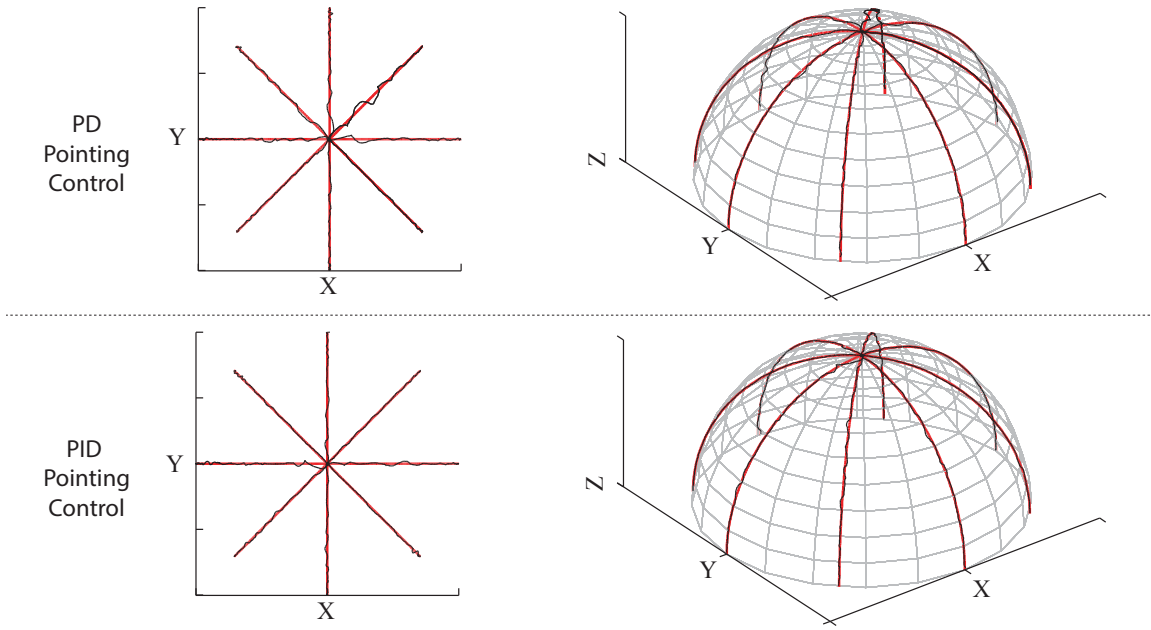


Figure 6.5. Quasi-static regulation experiments, repeated for both the PD and PID controllers. Each trial involved slowly rotating about a constant axis. Eight regularly spaced axes were chosen, spanning a hemisphere centered at $[0,0,1]^T$ at intervals of $\pi/4$ rad. Error data for each of the experiments are tabulated in Table 6.3.

Table 6.3. Tabulation of RMS errors accrued on each of the eight trials involving the quasi-static regulation experiment shown in Fig. 6.5. The alignment parameter in the table indicates the axis of revolution being evaluated with an alignment of 0 corresponding to the trial that rotates about $[1,0,0]^T$ and an alignment of $\pi/2$ corresponding to the trial that rotates about $[0,1,0]^T$.

Alignment (rad)	0	$\pi/4$	$\pi/2$	$3\pi/4$	π	$5\pi/4$	$3\pi/2$	$7\pi/4$
PD RMS Error (mrad)	31.1	33.0	26.1	23.4	24.9	29.9	33.3	37.0
PID RMS Error (mrad)	18.8	14.1	18.9	14.6	18.5	20.5	16.7	16.8

such that the dipole moved at a constant angular-velocity magnitude throughout. Two speeds were chosen to demonstrate the effect of speed on the system's tracking ability: a “fast” trajectory at a constant angular-velocity magnitude of 0.785 rad/s (where each circuit took 5.35s) and a “slow” trajectory at 0.393 rad/s (where each circuit took 10.7s). Both experiments performed five circuits of the figure-8 trajectory.

The results of both trajectories using the PD controller is shown in Fig. 6.6, and the results of using the PID controller on the same trajectories is shown in Fig. 6.7. On both the fast and the slow trajectory, both control methods evaluated perform comparably. On the fast trajectory, the PD controller yields an RMS error of 124.1 mrad, whereas the PID

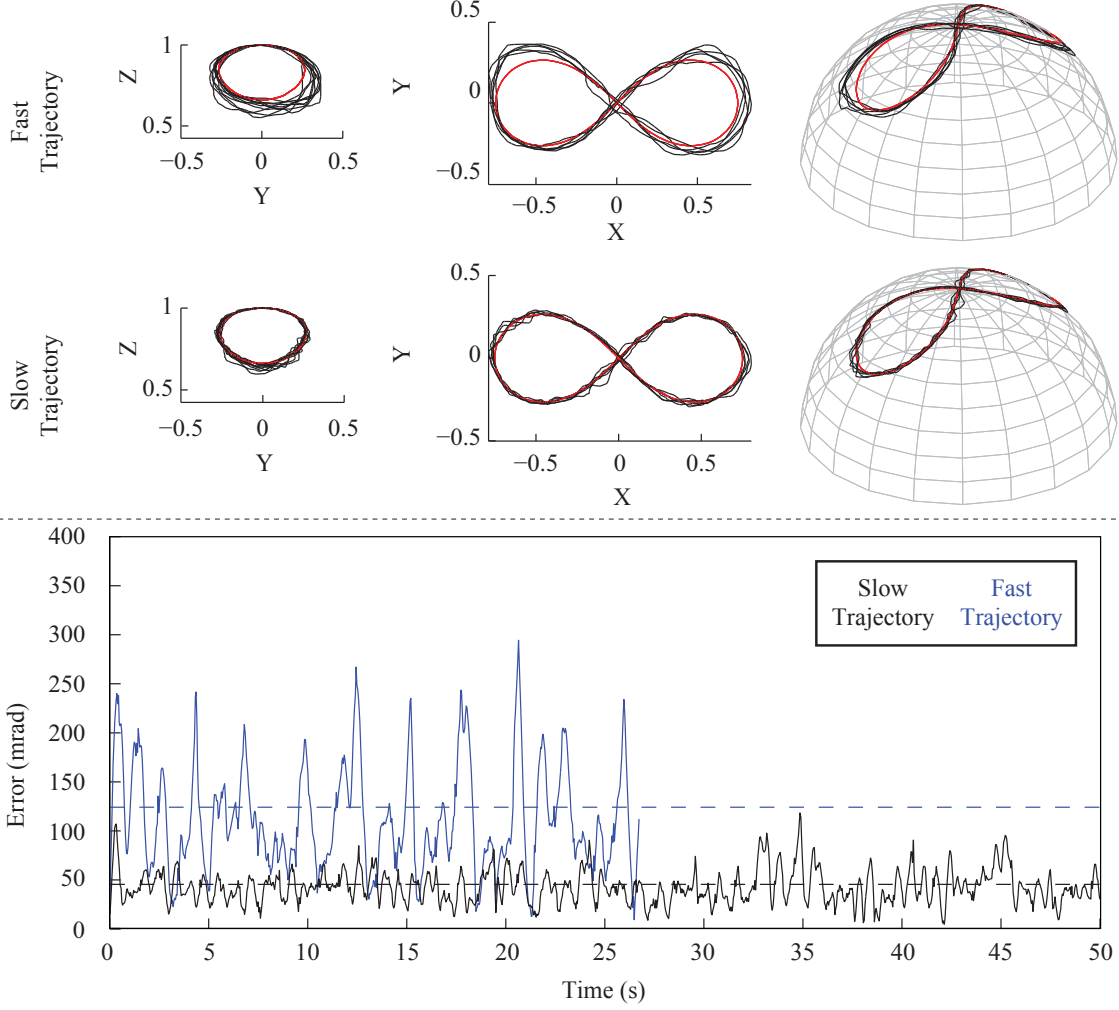


Figure 6.6. Results of tracking along five circuits of a “figure-8” trajectory at constant angular-velocity magnitudes of 0.785 rad/s and 0.393 rad/s using the PD controller tuned to the gains listed in Table 6.1. The fast and slow trajectories resulted in RMS errors of 124.1 and 45.8 mrad, respectively.

controller yields an RMS error of 127.0 mrad, which constitutes only a small difference. Similarly, on the slow trajectory, the PD controller yields an RMS error of 45.8 mrad, whereas the PID controller yields an RMS error of 45.2 mrad, which is again a small difference. Because of the small quantitative difference between PD and PID controllers observed in these trajectory-tracking experiments and the superior performance of the PID controller in the quasi-static experiments, we conclude that the PID controller is the appropriate controller to be used in the pointing-mode controller, as conjectured.

To further characterize the performance of the SAMM under PID pointing-control, an experimental closed-loop Bode plot was created and is shown in Fig. 6.8. The experiment

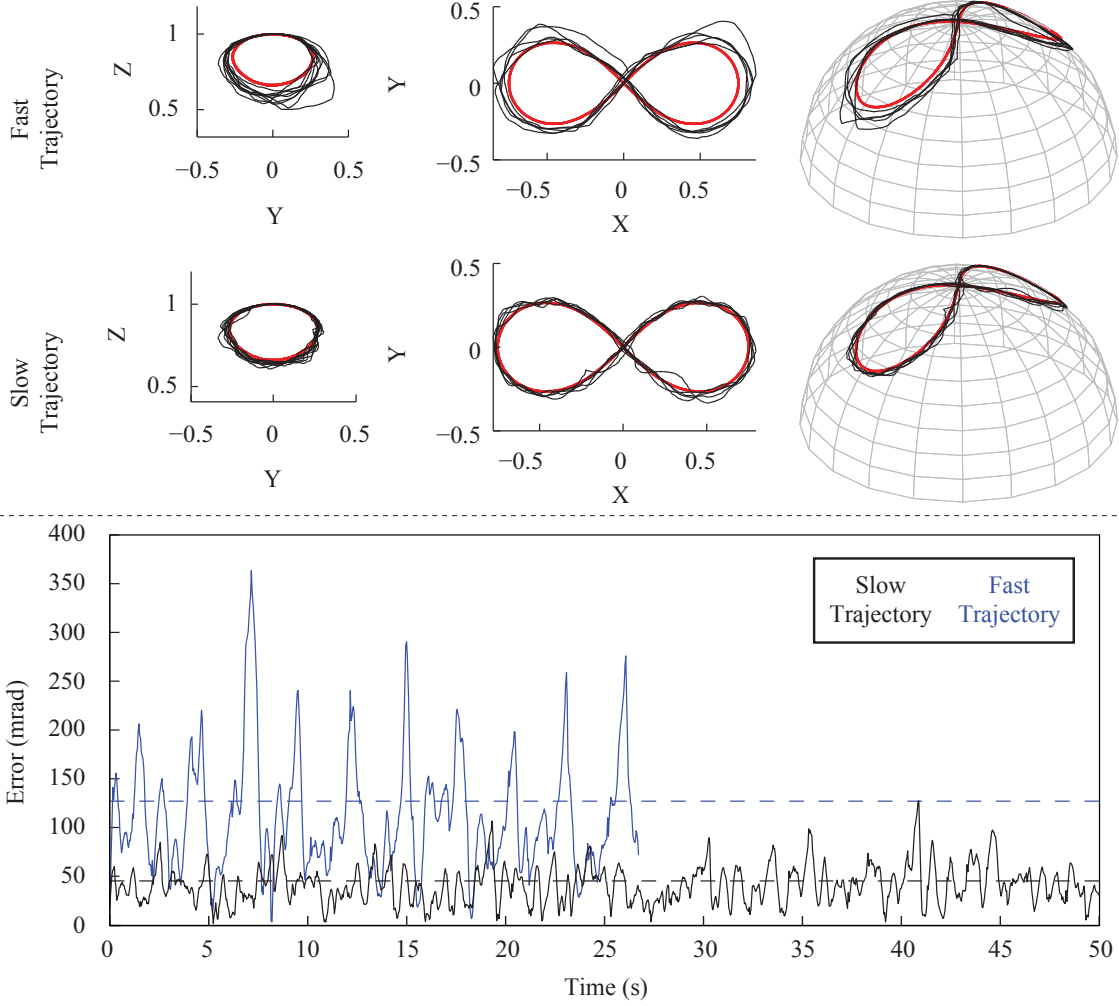


Figure 6.7. Results of tracking along five circuits of a “figure-8” trajectory at constant angular-velocity magnitudes of 0.785 rad/s and 0.393 rad/s using the PID controller tuned to the gains listed in Table 6.1. The fast and slow trajectories resulted in RMS errors of 127.0 and 45.2 mrad, respectively.

was performed in the direction of omniwheel axis $\hat{\mathbf{a}}_2$, removing any confounding effects of gearbox backlash. A Bode plot provides frequency-specific measurements of magnitude M (measured in dB) and phase ϕ (measured in degrees). This is accomplished by supplying the SAMM with a sinusoidal input of $a_{\text{in}}\sin(\omega_{\text{m}}t)$, where a_{in} is the input amplitude. The output trajectory of the SAMM is recorded and, using the *Curve Fitting* toolbox in MATLAB, a sinusoidal wave is fit in the form of $a_{\text{out}}\sin(\omega_{\text{m}}t + \phi)$. The magnitude is then computed as

$$M = 20\log\left(\frac{a_{\text{out}}}{a_{\text{in}}}\right). \quad (6.4)$$

This procedure was performed for the input amplitude $a_{\text{in}} = 5^\circ$ for 15 evenly spaced

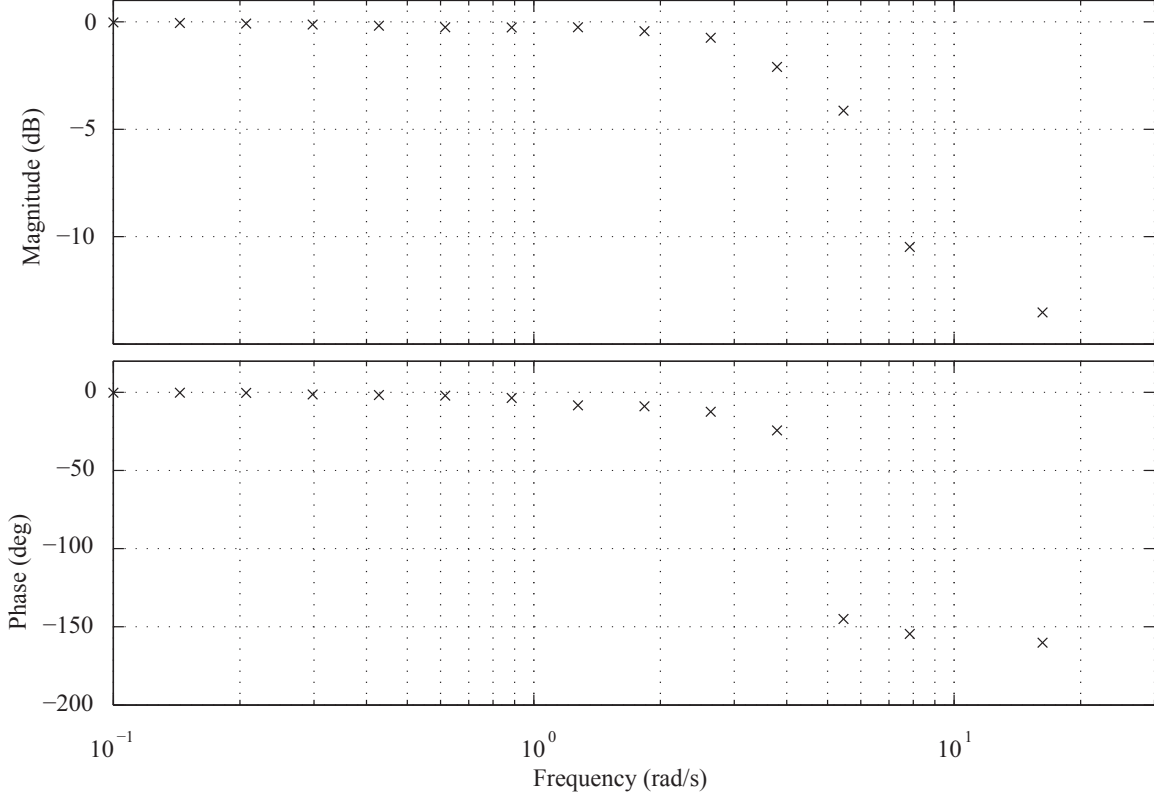


Figure 6.8. Experimental Bode plot of the PID pointing-mode controller using an input amplitude of $a_{\text{in}} = 5^\circ$.

frequencies (in log space) beginning at 0.1 rad/s through 16.2 rad/s.

The results of the closed-loop PID pointing-control experiments, shown in Fig. 6.8, demonstrate a corner frequency of approximately 3 rad/s. This frequency represents the point where faster frequencies becomes increasingly attenuated, and slower frequencies pass through largely unimpeded. It should be noted that, due to the nonlinear property of the SAMM, the demonstrated results are not generalizeable and are specific to the demonstrated input amplitude.

6.3.2 Rotating Mode

Two experiments are provided to demonstrate the rotating-mode operation. The first experiment shows the dipole's starting orientation aligned off the desired rotation plane, and tracks the dipole's heading as it aligns with the desired rotation plane while rotating about the desired angular-velocity input. The second experiment illustrates the case where the rotation axis is parallel with one of the omniwheel axes, resulting in one omniwheel primarily responsible for the net rotation and leaving the other two omniwheels to purely

perform regulation of the dipole to the plane. All experiments begin with the system at rest, and the dipole is controlled using the rotating-mode controller described in Section 5.2.

The rotating-mode controller consists of two orthogonal subcontrollers, each individually tuned. The rotation-plane heading subcontroller uses the same PD controller gains listed in Table 6.1. The Pessen-integral PID controller was briefly evaluated as a candidate controller for this task, but was ruled out due to poor performance, likely due to the speed at which this controller must react to disturbances. The angular-velocity subcontroller employs a PI-plus-feedforward controller as described in Section 5.2, tuned as described in Sec. 6.2.2.

For the first demonstration of the rotating mode, $\boldsymbol{\kappa} = \pi \cdot [\sqrt{2}/2, 0, \sqrt{2}/2]^T$ rad/s was chosen as the desired rotational velocity, as it is not aligned with any of the omniwheel axes, and the dipole was initialized at $[0, 0, 1]^T$, which is significantly off the desired rotation plane. The trajectory of the dipole can be viewed from multiple angles in Fig. 6.9. In this test, the dipole heading is aligned with the desired rotation plane within its first revolution about $\boldsymbol{\kappa}$. The error, both relative to the rotation plane and rotation axis, are illustrated in Fig. 6.10.

In the second experiment, the rotation axis of $\boldsymbol{\kappa} = \pi \cdot [\sqrt{2}/2, \sqrt{2}/2, 0]^T$ rad/s was chosen because it lies parallel with omniwheel axis $\hat{\mathbf{a}}_1$. Because of this, the majority of the work, apart from disturbance rejection, should be performed by omniwheel axis $\hat{\mathbf{a}}_1$. In addition, the dipole heading was initialized on the desired rotation plane, removing the transient effects and allowing the regulation performed by omniwheels $\hat{\mathbf{a}}_2$ and $\hat{\mathbf{a}}_3$ to be directly evaluated. The trajectory traced out by the dipole heading in this test is shown in Fig. 6.11. The rotation-plane and angular-velocity errors are shown in Fig. 6.12, as well as a plot illustrating the motor-space control effort, which confirms the expectation of omniwheel axis $\hat{\mathbf{a}}_1$ performing the primary control effort, while the other axes make smaller regulatory adjustments to hold the dipole on the rotation plane. These small adjustments never decay away to zero, but reach a steady-state in which the dipole is held within 3° of the intended plane.

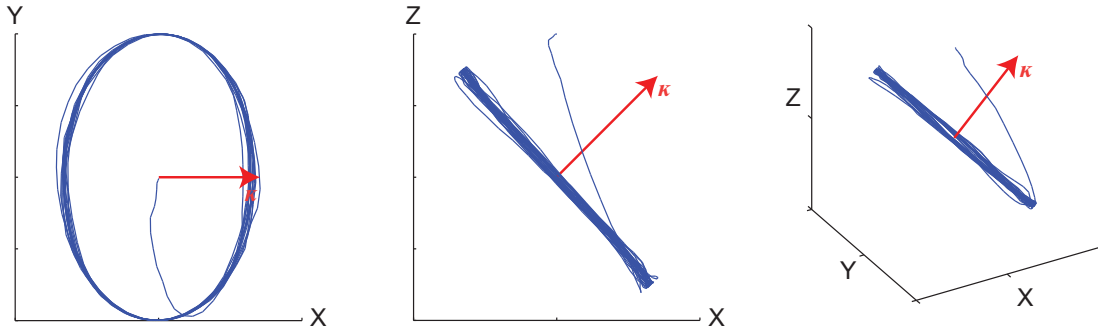


Figure 6.9. Recorded dipole heading while starting $[0,0,1]^T$ and being commanded to rotate about $\kappa = \pi \cdot [\sqrt{2}/2, 0, \sqrt{2}/2]^T$ rad/s. The experiment lasts 30 seconds, during which time the dipole heading aligns itself along the rotation plane while simultaneously rotating about κ .

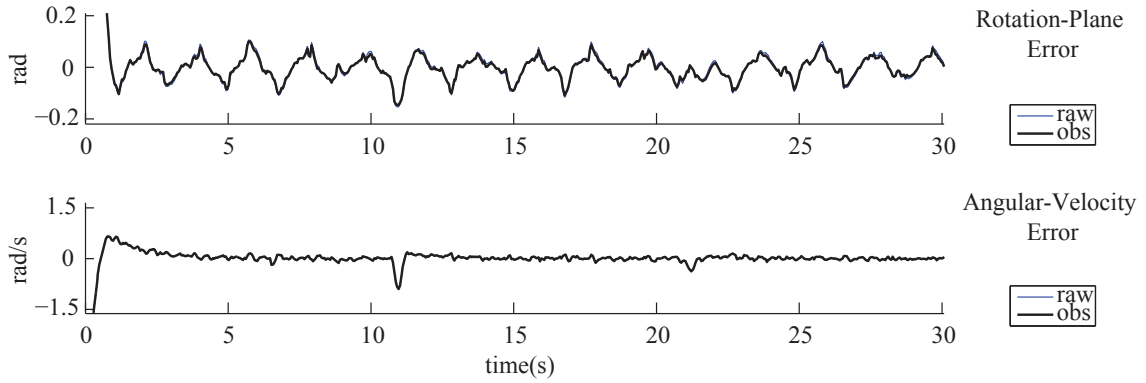


Figure 6.10. Recorded errors corresponding to trajectory shown in Fig. 6.9. (Top) The rotation-plane error plot illustrates the rotation-plane heading subcontroller with RMS error of 0.0347 rad for the final 50% of the test. (Bottom) The angular-velocity error plot illustrates the PI-plus-feedforward angular-velocity subcontroller with RMS error of 0.070 rad/s for the final 50% of the test.

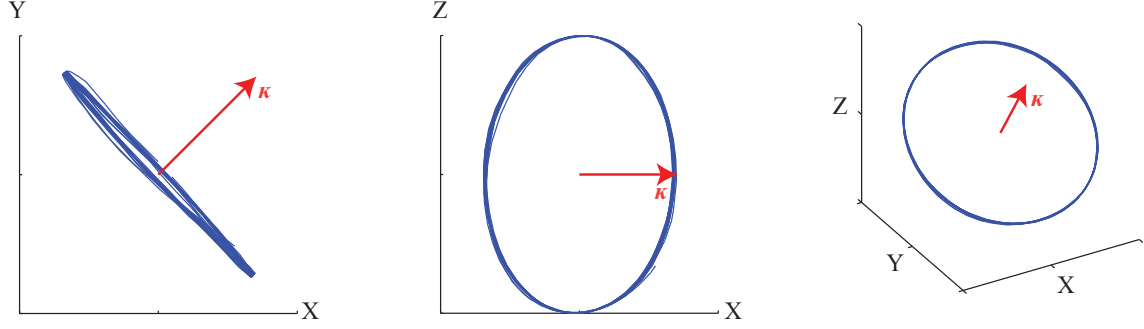


Figure 6.11. Path of the SAMM's dipole heading while rotating about $\kappa = \pi \cdot [\sqrt{2}/2, \sqrt{2}/2, 0]^T$ rad/s, which lies parallel to omniwheel axis $\hat{\mathbf{a}}_1$. The experiment begins with the dipole heading closely aligned with the desired rotation plane.

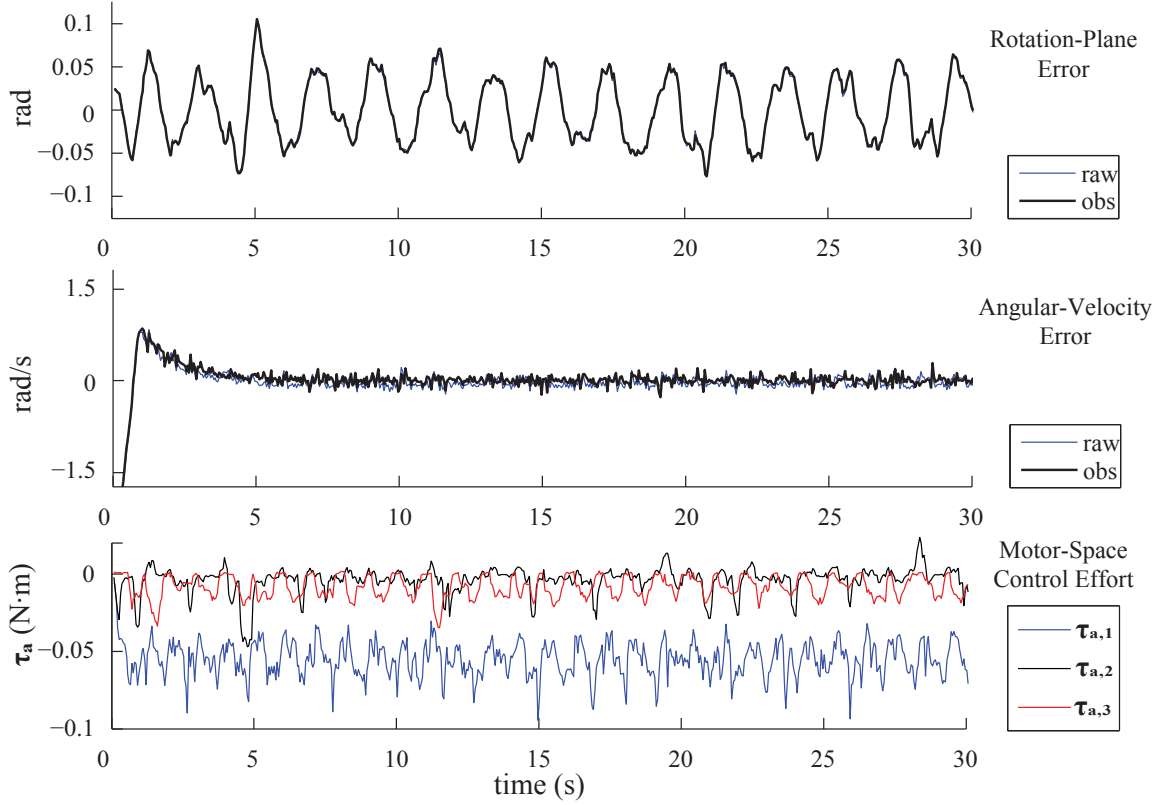


Figure 6.12. Recorded errors corresponding to trajectory shown in Fig.6.11. (Top) Rotation-plane error plot shows the orthogonal heading subcontroller working to keep the dipole heading on the intended rotation plane, with an RMS error of 0.0372 rad. (Middle) Angular-velocity error plot shows the PI-plus-feedforward subcontroller working to maintain the dipole's intended angular-velocity κ with an RMS error of 0.0716 rad/s for the final 50% of the data. (Bottom) The motor-space control effort illustrates that omniwheel axis $\hat{\mathbf{a}}_1$ does perform the primary control effort, while the other axes stabilize the dipole heading on the desired plane.

CHAPTER 7

DISCUSSION

7.1 Spherical-magnet Substitution

In place of a spherical magnet, permanent magnets of arbitrary shapes may be embedded in a spherical body as illustrated in Figs. 7.1(b–c). However, a spherical magnet has many clear benefits over embedding magnets of other geometries within a sphere. First, a spherical magnet maximizes the volume of magnetic material within the bounding sphere. Additionally, it maximizes the fit of the magnetic field to the analytical point-dipole model (2.10). Finally, a homogeneous spherical body has isotropic mechanical properties; other shapes may require additional knowledge of the embedded magnetic body’s orientation to properly model the dynamics. Additional care must be taken to properly center the embedded magnet’s center of mass with the center of the sphere to prevent vibrations at higher angular velocities. Because of the potential for undesirable vibrations, poorer fit to the point-dipole model, weaker field, and fabrication challenges, it is not advisable to embed magnets of other geometries within a spherical body, given that the designer has access to commercially available spherical magnets.

7.2 Application-specific Tuning of the Gear Ratio η

For the prototype SAMM described in Chapter 3, omniwheels of 58.2-mm diameter were chosen in conjunction with a 50.8-mm-diameter magnet, resulting in a gear ratio of $\eta = -0.873$. This results in a spherical-magnet angular velocity that is higher than the motor’s output angular velocity at the cost of lower torque available to the magnet for disturbance rejection.

In future instantiations, where application permits, this gear ratio could be used to tune the SAMM’s dynamics. For example, the same size omniwheels could be used with a 102-mm-diameter magnet to create a gear ratio of $\eta = -1.75$. This new SAMM, when given the same motor angular velocity as the current SAMM, would result in a slower,

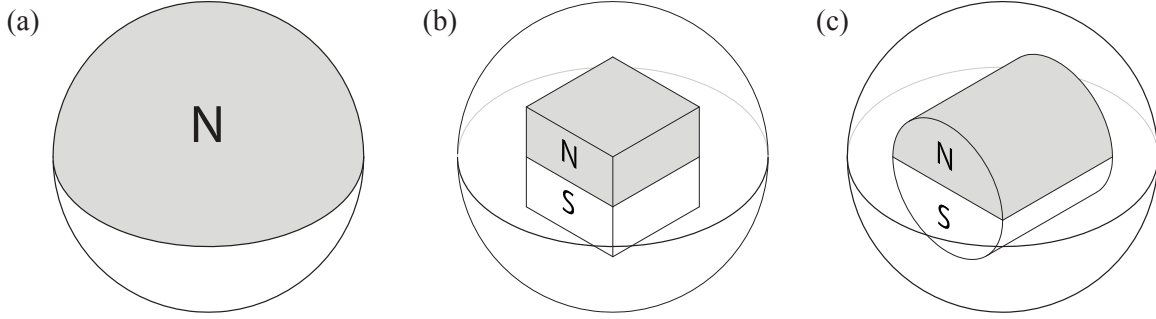


Figure 7.1. The spherical magnetic body can be a spherical permanent magnet (a), or it can be a permanent magnet of any other geometry, such as a cube (b) or cylinder (c), encapsulated in a spherical structure.

more precise spherical magnet, with more torque available to the magnet for disturbance rejection.

In other applications, where a nonisotropic design may be desirable, omniwheels of different diameters may be used on a single SAMM. This would replace the scalar η defined in (2.6) with the diagonal matrix

$$\boldsymbol{\eta} = \text{diag} \left(\begin{bmatrix} -r_m/r_{w1} \\ -r_m/r_{w2} \\ -r_m/r_{w3} \end{bmatrix} \right) = \begin{bmatrix} \eta_1 & 0 & 0 \\ 0 & \eta_2 & 0 \\ 0 & 0 & \eta_3 \end{bmatrix}. \quad (7.1)$$

7.3 Omniwheel Orientations

The prototype SAMM described in Chapter 3 is an example of the “counteropposed” omniwheel configuration, shown in Fig. 2.1(a). This configuration allows the normal force from each omniwheel to be held by the other opposing omniwheels, subsequently increasing their traction. This, however, is just one of many valid configurations that do not violate any of the assumptions made in Chapter 2. For example, Fig. 2.1(b) illustrates a configuration that increases the usable workspace, but at the cost of inefficient normal-force distribution. The configurations similar to Fig. 2.1(c) increase the usable workspace further, but it may become mechanically complex to actuate the omniwheels.

7.4 Potential Performance Improvements

Every effort was made to make the prototype demonstrated in Chapter 6 as high-performing as possible. Despite this there are many avenues of improvement to explore for future instantiations of the SAMM.

7.4.1 SAMM Components

A primary constraint in fabricating the SAMM was the requirement that components be nonmagnetic. Some assembly components were commercially available in nonmagnetic form, others had to be custom manufactured. For example, the 90° gearboxes were purchased with the intent of retrofitting with nonmagnetic components. The internal steel bevel gears were replaced with Nylon 6/6 replacements, custom axles were machined out of 7075 aluminum, and the steel ball-bearings were replaced with polyacetal versions. This yielded a nonmagnetic 90° gearbox, but introduced axial play in the input and output shafts, higher rotating friction, and backlash into the kinematics of the gearboxes.

The Maxon Motor drives that were employed provide feedback of the motor’s angular velocity and the supplied current to the SAMM for state estimation. Unfortunately, the provided signals are quite noisy, so much so that these are likely the largest source of noise in the system. The Kalman observer is capable of filtering the signals to make useful state estimates, but this noise is visible in the angular-velocity estimate. Hardware filtering or other drivers could be explored in future SAMM instantiations.

7.4.2 Further Empirical Tuning

Omniwheel axes $\hat{\mathbf{a}}_i$ are assumed ideal in the prototype SAMM. Similarly, the sensing directions $\hat{\mathbf{v}}_i$, sensor positions \mathbf{p}_i , and Hall-effect sensor sensitivities are not calibrated. Additionally, the spherical magnet is assumed ideal in its magnetization strength and distribution. Errors in any of these assumptions could introduce disturbances into the system and effect the accuracy of the state estimation. Empirical calibration of such parameters using techniques such as *System Identification*, *Expectation Maximization*, and mechanical calibration could form a more accurate estimate of the SAMM’s parameters.

CHAPTER 8

CONCLUSION

This thesis presented the design, assembly, state-estimation, and control of a 3-DOF mechatronic device to rotate a spherical, or spherically encapsulated, permanent magnet for the control of remote magnetic devices. We dubbed the mechatronic device the spherical-actuator-magnet manipulator (SAMM). The SAMM was conceived to replace or augment the singularity-prone spherical wrist used by prior permanent-magnet manipulation systems. The SAMM performs 3-DOF holonomic singularity-free control of the spherical magnet's heading, and allows the magnet's instantaneous axis-of-rotation to be set arbitrarily. It accomplishes this by driving a spherical magnet by way of three mutually orthogonal omni-wheels. The SAMM was fabricated out of nonmagnetic components, with exception of the DC motors, which were located far from the spherical magnet. Nonconductive components were preferred for components with large volumes to reduce eddy-current disturbances. The SAMM utilizes real-time sensory feedback of the magnetic dipole heading via a cluster of Hall-effect sensors and angular velocity via incremental optical encoders attached to the motors. A hybrid extended Kalman filter was developed to perform sensor-fusion and state estimation. Closed-loop control was demonstrated illustrating pointing and angular-velocity control of the spherical magnet's dipole.

REFERENCES

- [1] B. J. Nelson, I. K. Kaliakatsos, and J. J. Abbott, "Microrobots for minimally invasive medicine," *Annu. Rev. Biomed. Eng.*, vol. 12, pp. 55–85, 2010.
- [2] J. L. Toennies, G. Tortora, M. Simi, P. Valdastri, and R. J. Webster III, "Swallowable medical devices for diagnosis and surgery: the state of the art," *J. Mech. Eng. Sci.*, vol. 224, no. 7, pp. 1397–1414, 2010.
- [3] G. Ciuti, P. Valdastri, A. Menciassi, and P. Dario, "Robotic magnetic steering and locomotion of capsule endoscope for diagnostic and surgical endoluminal procedures," *Robotica*, vol. 28, no. 2, pp. 199–207, 2010.
- [4] M. P. Kummer, J. J. Abbott, B. E. Kratochvil, R. Borer, A. Sengul, and B. J. Nelson, "OctoMag: an electromagnetic systems for 5-DOF wireless micromanipulation," *IEEE Trans. Robot.*, vol. 26, no. 6, pp. 1006–1017, 2010.
- [5] M. T. Hou, H. -M. Shen, G. -L. Jiang, C. -N. Lu, I -J. Hsu, and J. A. Yeh, "A rolling locomotion method for untethered magnetic microrobots," *Appl. Phys. Lett.*, vol. 96, no. 024102, pp. 1–3, 2010.
- [6] S. Yim and M. Sitti, "Design and rolling locomotion of a magnetically actuated soft capsule endoscope," *IEEE Trans. Robot.*, vol. 28, no. 1, pp. 183–194, 2012.
- [7] A. W. Mahoney and J. J. Abbott, "Managing magnetic force applied to a magnetic device by a rotating dipole field," *Appl. Phys. Lett.*, vol. 99, no. 134103, pp. 1–3, 2011.
- [8] T. W. R. Fountain, P. V. Kailat, and J. J. Abbott, "Wireless control of magnetic helical microrobots using a rotating-permanent-magnet manipulator," in *Proc. IEEE Int. Conf. Robot. Automation*, 2010, pp. 576–581.
- [9] J. -S. Lee, B. Kim, and Y. -S. Hong, "A flexible chain-based screw propeller for capsule endoscopes," *Int. J. Prec. Eng. Manuf.*, vol. 10, no. 4, pp. 27–34, 2009.
- [10] A. Ghosh and P. Fischer, "Controlled propulsion of artificial magnetic nanostructured propellers," *Nano Lett.*, vol. 9, no. 6, pp. 2243–2245, 2009.
- [11] M. Sendoh, K. Ishiyama, and K. I. Arai, "Fabrication of magnetic actuator for use in a capsule endoscope," *IEEE Trans. Magn.*, vol. 39, no. 5, pp. 3232–3234, 2003.
- [12] L. Zhang, J. J. Abbott, L. X. Dong, B. E. Kratochvil, D. Bell, and B. J. Nelson, "Artificial bacterial flagella: fabrication and magnetic control," *Appl. Phys. Lett.*, vol. 94, no. 064107, pp. 1–3, 2009.
- [13] K. Ishiyama, K. I. Arai, M. Sendoh, and A. Yamazaki, "Spiral-type micro-machine for medical applications," *J. Micromechatronics*, vol. 2, no. 1, pp. 77–86, 2003.

- [14] A. W. Mahoney and J. J. Abbott, "Generating rotating magnetic fields with a single permanent magnet for propulsion of untethered magnetic devices in a lumen," *IEEE Trans. Robot.*, vol. 30, no. 2, pp. 411–420, 2014.
- [15] A. W. Mahoney and J. J. Abbott, "5-DOF manipulation of a magnetic capsule in fluid using a single permanent magnet: proof-of-concept for stomach endoscopy," in *Proc. 6th Hamlyn Symp. Med. Robot.*, 2013, pp. 114–115.
- [16] A. W. Mahoney and J. J. Abbott, "5-DOF manipulation of an untethered magnetic device in fluid using a single permanent magnet," in *Proc. Robotics: Science Systems*, Berkeley, USA, July 2014.
- [17] G. T. Gillies, R. C. Ritter, W. C. Broaddus, M. S. Grady, M. A. Howard III, and R. G. McNeil, "Magnetic manipulation instrumentation for medical physics research," *Rev. Sci. Instrum.*, vol. 65, no. 3, pp. 533–562, 1994.
- [18] J. R. Clark, L. Leon, F. M. Warren, and J. J. Abbott, "Magnetic guidance of cochlear implants: proof-of-concept and initial feasibility study," *J. Med. Devices*, 2012.
- [19] M. Kumaga and T. Ochiai, "Development of a robot balanced on a ball: Application of passive motion to transport," in *Proc. IEEE Int. Conf. Robot. Automation*, 2009, pp. 4106–4111.
- [20] T. B. Lauwers, G. A. Kantor, and R. L. Hollis, "A dynamically stable single-wheeled mobile robot with inverse mouse-ball drive," in *Proc. IEEE Int. Conf. Robot. Automation*, 2006, pp. 2884–2889.
- [21] U. Nagarajan, G. Kantor, and R. Hollis, "The ballbot: An omnidirectional balancing mobile robot," *Int. J. Robot. Res.*, vol. 33, no. 6, pp. 917–930, 2014.
- [22] M. Kumaga and R. L. Hollis, "Development of a three-dimensional ball rotation sensing system using optical mouse sensors," in *Proc. IEEE Int. Conf. Robot. Automation*, 2011, pp. 5038–5043.
- [23] Rezero, "Focus project ballbot," 2014, Available: <http://www.rezero.ethz.ch>.
- [24] K. -S. Byun and J. -B. Song, "Design and construction of continuous alternate wheels for an omnidirectional mobile robot," *J. Robot. Sys.*, vol. 20, no. 9, pp. 569–579, 2003.
- [25] E. P. Furlani, *Permanent magnet and electromechanical devices: materials, analysis, and applications*, 1st ed. San Diego, CA: Academic Press, 2001.
- [26] A. J. Petruska and J. J. Abbott, "Optimal permanent-magnet geometries for dipole field approximation," *IEEE Trans. Magn.*, vol. 49, no. 2, pp. 811–819, 2013.
- [27] R. A. Horn and C. R. Johnson, *Matrix Analysis*, 2nd ed. Cambridge, UK: Cambridge University Press, 1985.
- [28] R. L. Norton, *Design of Machinery*, 5th ed. New York, NY: McGraw Hill, 2012.
- [29] S. Thrun, W. Burgard, and D. Fox, *Probabilistic Robotics*, 1st ed. Cambridge, MA: MIT Press, 2006.
- [30] D. Simon, *Optimal State Estimation*, 1st ed. Hoboken, NJ: John Wiley & Sons, 2006.

- [31] H. Olsson, K. J. Åström, C. Canudas de Wit, M. Gäfvert, and P. Lischinsky, “Friction Models and Friction Compensation,” *Eur. J. Cont.*, vol. 4, no. 3, pp. 176–195, 1998.
- [32] D. W. Pessen, “A New Look at PID-Controller Tuning,” *J. Dyn. Sys., Meas., Cont.*, vol. 116, pp. 553–557, 1994.